A combined sea and sea-ice surface temperature climate dataset of the Arctic, 1982–2021

Nielsen-Englyst, Pia; Høyer, Jacob L.; Kolbe, Wiebke M.; Dybkjær, Gorm; Lavergne, Thomas; Tonboe, Rasmus Tage; Skarpalezos, Sotirios; Karagali, Ioanna

Published in:
Remote Sensing of Environment

Link to article, DOI:
10.1016/j.rse.2022.113331

Publication date:
2023

Document Version
Publisher's PDF, also known as Version of record

Remote Sensing of Environment 284 (2023) 113331

Contents lists available at ScienceDirect

Remote Sensing of Environment

journal homepage: www.elsevier.com/locate/rse

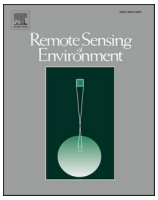

A combined sea and sea-ice surface temperature climate dataset of the Arctic, 1982–2021

Pia Nielsen-Englyst [a,b,*], Jacob L. Høyer [b], Wiebke M. Kolbe [a,b], Gorm Dybkjær [b], Thomas Lavergne [c], Rasmus Tage Tonboe [a], Sotirios Skarpalezos [b], Ioanna Karagali [b]

[a] DTU-Space, Technical University of Denmark, DK-2800 Lyngby, Denmark
[b] National Centre for Climate Research, Danish Meteorological Institute, Lyngbyvej 100, DK-2100 Copenhagen Ø, Denmark
[c] Research and Development Department, Norwegian Meteorological Institute, Oslo, Norway

ARTICLE INFO

Editor: Menghua Wang

Keywords:
Arctic
Sea surface temperature
Sea ice surface temperature
Infrared satellite observations
Optimal interpolation
Climate change

ABSTRACT

The surface temperature is one of the main parameters for assessing climate change. Temperature change is most pronounced in the Arctic, and therefore, it is crucial to accurately estimate sea and sea ice surface temperatures in this region. The availability of in situ observations is limited in the Arctic, thus, increasing the need for satellite observations to estimate surface temperatures. We present the first Arctic (>58°N) gap-free climate dataset covering the surface temperatures of the ocean, sea ice and the marginal ice zone from 1 January 1982 to 31 May 2021 based on observations from infrared satellite sensors. The underlying algorithm combines the multi-satellite observations and performs a statistical optimal interpolation to obtain daily gap-free fields, with a spatial resolution of 0.05° in latitude and longitude. In situ observations have been used to derive consistent validation statistics over the ocean and sea ice. Comparison of the derived sea surface temperatures against in situ measurements from drifting buoys, moored buoys and Argo floats shows mean differences of 0.01 °C, 0.04 °C and 0.04 °C and standard deviations of 0.54 °C, 0.56 °C and 0.51 °C, respectively. Over sea ice, the derived ice surface temperatures have been compared with KT-19 measurements from IceBridge flights, showing a mean difference of 1.52 °C and standard deviation of 3.12 °C, and with air temperatures from the North Pole (NP) ice drifting stations as well as ECMWF distributed buoys and CRREL buoys, with mean differences of −2.35 °C, −3.21 °C and −2.87 °C and standard deviations of 3.12 °C, 3.34 °C and 3.36 °C, respectively. The combination of sea and sea-ice surface temperature provides a consistent dataset for climate analysis, which is crucial for studying climate change and trends in the Arctic. The combined sea and sea-ice surface temperature of the Arctic has risen with about 4.5 °C over the period 1982–2021, with a peak warming of around 10 °C in the northeastern Barents Sea.

1. Introduction

The surface temperature is one of the main variables for assessing climate change (Bates and Diaz, 1991; Bojinski et al., 2014; Folland et al., 2001; Kaplan et al., 1998). This is also true for the Arctic, where positive feedback mechanisms, e.g. the ice-albedo feedback, amplify climate change (AMAP, 2021; Comiso and Hall, 2014; Graversen et al., 2008; Hall et al., 2004; IPCC, 2019; Pithan and Mauritsen, 2014; Rantanen et al., 2022; Richter-Menge et al., 2017). In the Arctic Ocean, the surface temperatures play a crucial role for the heat exchange between the ocean and atmosphere, sea ice growth and melt processes (Key et al., 1997; Maykut, 1986) as well as in weather and sea ice forecasts through assimilation into ocean and atmospheric models (Carton et al., 2000; Larsen et al., 2007; Oke et al., 2008; Rasmussen et al., 2018; Rayner, 2003; Song and Yu, 2012). Therefore, it is important to accurately estimate the surface temperature of the Arctic Ocean, which consists of open ocean, sea ice and a marginal ice zone (MIZ), i.e. the transitional region between the open ocean and pack ice. The extreme environment and the poor accessibility (especially in the winter season) make in situ observations challenging and sparse in the Arctic (Centurioni et al., 2019; Donlon et al., 2012). Polar orbiting satellites offer a very good alternative and addition to the in situ observations through their high spatial and temporal coverage of the Arctic.

A large number of global gap-free (optimally interpolated) gridded

* Corresponding author at: DTU-Space, Technical University of Denmark, DK-2800 Lyngby, Denmark.
E-mail address: pne@dmi.dk (P. Nielsen-Englyst).

https://doi.org/10.1016/j.rse.2022.113331
Received 1 April 2022; Received in revised form 14 September 2022; Accepted 26 October 2022
Available online 12 November 2022

sea surface temperature (SST) products (Level 4, L4, analyses) have been developed based on a variety of different satellite observations and sometimes including in situ observations as well (Donlon et al., 2012; Good et al., 2020; Merchant et al., 2014, 2019; Reynolds et al., 2002, 2007; Roberts-Jones et al., 2012). Differences are known to exist among the analyses due to varying input data (both infrared and microwave satellite and in situ), quality control procedures, cloud-masks, land/ice masks, interpolation techniques and related configurations (e.g. correlation scales and grid sizes). Several inter-comparison studies have been performed to understand the consistency and discrepancy of the different L4 SST analyses (Dash et al., 2012; Fiedler et al., 2019; Martin et al., 2012; Okuro et al., 2014; Yang et al., 2021). The L4 SST analyses perform fairly uniformly globally, with accuracies better than 0.5 °C in clear-sky conditions (Martin et al., 2012; Petrenko et al., 2014; Wang et al., 2016), but large uncertainties and significant differences are found at high latitudes in particular in coastal and dynamic regions (Castro et al., 2016; Dash et al., 2012; Vazquez-Cuervo et al., 2022). The extreme atmospheric and oceanographic conditions, sparsely distributed in situ observations, and persistent cloud cover complicate accurate SST satellite retrievals in the Arctic (Donlon et al., 2010; Høyer et al., 2012). Specialized high latitude algorithms have been developed and shown to outperform the global analyses in these regions (Jia and Minnett, 2020; Vincent et al., 2008a, 2008b). Improving the SST data quality in the Arctic has been identified by the SST community as being of high priority for future SST research and developments (O'Carroll et al., 2019).

The presence of both seawater and ice, and the large seasonal and inter-annual fluctuations in the sea ice cover, lead to increased complexity in the SST mapping of the Arctic region. Traditionally, global gridded SST products use independent satellite observed sea ice concentration (SIC) to derive an ice mask. Few products simply do not report SST in ice covered waters, while most products provide a foundation or mixed layer temperature of the sea water just below the ice, which is assumed to be at the freezing point of seawater (−1.8 °C for salinities around 35 psu) for high SICs. Different methods and empirical relationships have been used to generate proxy SSTs from SICs in the MIZ (Banzon et al., 2020), which in some cases are blended with the closest open water SSTs (Rayner, 2003; Reynolds et al., 2007, 2002).

However, the use of under ice SSTs in the MIZ and in sea ice covered regions does not represent the surface temperature as very large temperature gradients can exist through the sea ice and snow (Tonboe et al., 2011). These products cannot be used to estimate the surface heat exchange with the atmosphere, and thus, not appropriate for use as boundary conditions in e.g. atmospheric models or to assess the surface temperature changes in the Arctic Ocean. Combining SST and ice surface temperature (IST) is identified as the most appropriate method for determining the surface temperature of the Arctic (Minnett et al., 2019).

Ice surface temperature retrievals from satellites are based on thermal infrared (IR) data, which implies that satellite IST products represent clear sky temperatures. However, automatic cloud screening over Arctic sea ice is challenging due to the resemblance of ice and cloud top temperatures. Undetected clouds or atmospheric ice/water typically results in larger IST errors than for SST retrievals, including a cold bias (Dybkjær et al., 2012; Hall et al., 2004). A number of satellite-based IST products are available (Hall et al., 2004; Key et al., 1994, 1997, 2013; Maslanik et al., 1997) and some combine Arctic SST and IST (Dybkjær et al., 2012; Vincent et al., 2008b), while few products include land surface temperatures as well (Comiso, 2003; Comiso and Hall, 2014; Dodd et al., 2019). A Near-Real-Time (NRT) gap-free (all-sky) combined SST, IST and MIZT product (L4 SST/IST) has been produced for a few years within the Copernicus Marine Service (CMEMS; doi: https://doi.org/10.48670/moi-00130), however, no L4 SST/IST reanalysis or climate data record (CDR) has previously been generated for the Arctic Ocean, based on IR satellite observations. Significant differences in surface temperatures are observed during all-sky and clear-sky conditions (Nielsen-Englyst et al., 2019; Walsh and Chapman, 1998). Therefore, to study climate trends, it is important with an effective way to fill in the gaps (due to clouds) since inter-annual variations in cloud cover may impact the accuracy of the trends observed when only clear-sky data are used (Liu et al., 2008).

Previously, climate trends have been estimated individually for SST and IST records (e.g. (Bulgin et al., 2020; Comiso, 2003; Comiso and Hall, 2014; Merchant et al., 2019; Wang and Key, 2005). However, this is problematic in the Arctic region due to the large temporal variability in the sea ice cover including the overlying northward migration of the ice edge on decadal timescales, and thus, the resulting climate trends are not easy to interpret (Comiso, 2003). A combined surface temperature dataset of the ocean, sea ice and the MIZ provides a consistent climate indicator, which is important for studying climate trends in the Arctic region.

This paper presents the generation, validation and analysis of the first gap-free, combined sea and sea-ice surface temperature climate dataset, with CDR-like temporal consistency, for the Arctic (>58°N) covering the period from 1 January 1982 to 31 May 2021. It is based on IR satellite products of surface temperatures from the European Space Agency's Climate Change Initiative (ESA CCI), the Copernicus Climate Change Service (C3S) and the Arctic and Antarctic ice Surface Temperatures from thermal Infrared (AASTI). A multiplatform optimal interpolation (OI) scheme has been used to combine these data sources and fill the gaps due to clouds. It has been developed considering the conditions that apply in the Arctic with special attention to the MIZ, where it produces a combination of open water SST and IST. Each surface type (i.e. sea ice, open ocean and MIZ), has its own characteristics, and thus, it is very important with an accurate SIC product to identify the different regions. Because of this, a combination of several SIC products and additional filtering and consistency checks between the SST and SIC fields have been developed to reduce erroneous SIC observations and produce an improved SIC product in particular close to the coasts.

The paper is organized such that Section 2, describes the satellite and in situ data used for construction and validation of the dataset. In Section 3, the methods and processing steps of the SIC and the L4 SST/IST fields are described. The results, validation, and analysis of the L4 SST/IST are provided in Section 4, while discussion and conclusions are given in Section 5 and Section 6, respectively.

2. Data

Multiple sources of satellite observations are used over the sea and sea ice surfaces in the Arctic in order to provide IST and SST information for the L4 SST/IST processing. Fig. 1 shows the temporal coverage of the individual SST/IST satellite products used as input to the Danish Meteorological Institute Optimal Interpolation (DMIOI) L4 processing system and the in situ observations used for validation. Moreover, it shows the temporal coverage of the input SIC products and the auxiliary data used in the generation of the OI SIC product (see Section 3.a). Details about each data source are provided below.

2.1. Satellite data

2.1.1. Sea and sea ice surface temperature

2.1.1.1. SST CCI L2P. The SST CCI version 2.1 data are used for the period 1982–2016, and they are obtained through the ESA CCI project (Merchant et al., 2019). The SST CCI data include observations from the ATSR 1 instrument on board the ERS-1 satellite, ATSR 2 on board the ERS-2 satellite, and the AATSR on board ENVISAT, and the AVHRR on board the NOAA and Metop satellites. The CCI SST retrievals provide the temperature at 20 cm depth at the nearest of 10:30 h or 22.30 h local time to best represent the daily mean (Embury et al., 2012; Merchant et al., 2019).

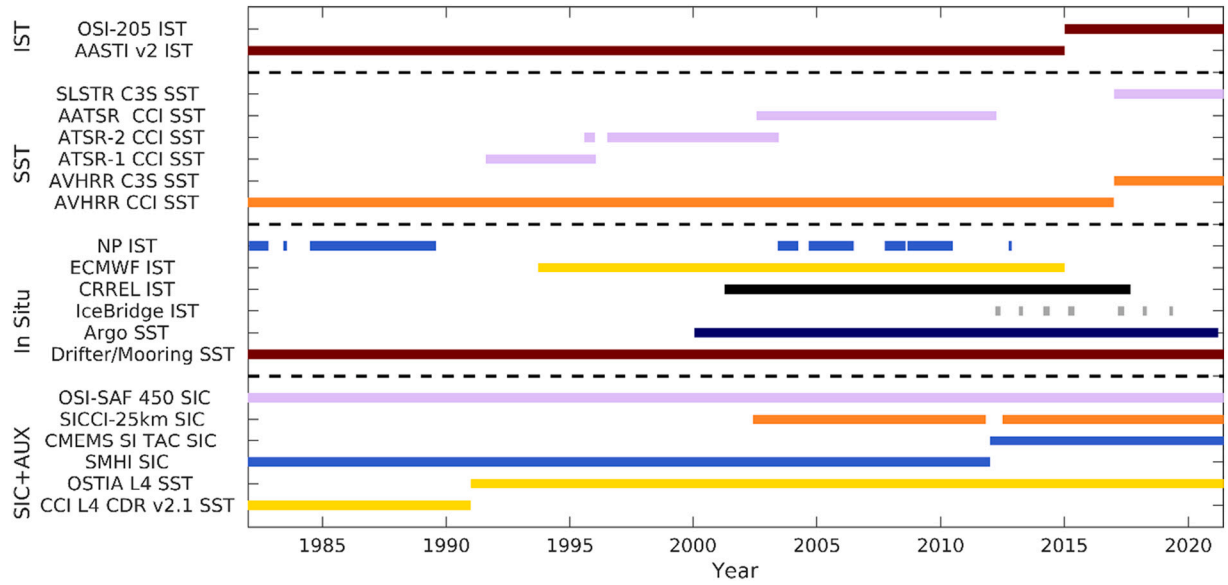

Fig. 1. Temporal coverage of the input satellite IST and SST data, the in situ IST and SST observations as well as the input SIC products and the auxiliary data used for the OI SIC generation.

2.1.1.2. C3S SST. For the period 2017–2021, SST observations from C3S are used. From 2017 to August 31, 2019, the C3S data are provided in satellite swath coordinates, referred to as Level 2 (L2), while the data are provided as gridded single L2 files, referred to as Level 3 uncollated (L3U) files after this period. The C3S data is obtained from Owen Embury (personal communication, 2018) and corresponds to the L3U data files available from https://cds.climate.copernicus.eu/ except for the higher spatial resolution. The C3S data include observations from the SLSTR A/B instruments on board the Sentinel 3 satellites and the AVHRRs on board the NOAA and Metop satellites.

2.1.1.3. AASTI + OSI-205 IST. IST observations are obtained by combining two data sources; a climate dataset and data from a NRT data stream. The Arctic and Antarctic ice Surface Temperatures from thermal Infrared satellite climate dataset version 2 (AASTI v2) covering the period 1982–2014 (Dybkjær et al., 2014, 2022) and data from the operational OSISAF IST product (OSI-205) covering the period from 2015 and onwards (Dybkjær et al., 2018). The AASTI and OSI-205 data are retrieved by identical algorithms from a single sensor type, the AVHRR sensors, where the applied algorithms are calibrated specifically for each sensor. The data format for the two datasets differ, as AASTI uses the Global Area Coverage (GAC) and the OSI-205 uses the Local Area Coverage (LAC), at approximately 4 and 1 km resolution, respectively. In Dybkjær et al. (2018) the retrieval system is described in detail.

A critical step for IST retrievals is the cloud detection procedure. For this purpose, the cloud mask from the EUMETSAT Nowcasting Satellite Application Facility (NWCSAF) Polar Platform System version 2014 (PPS2014) is used (Dybbroe et al., 2005a, 2005b; SMHI, 2014). The PPS has for years been used for automatic cloud masking for AVHRR and other sensors (Dybbroe et al., 2005b). However, cloud mask quality over ice during non-sunlit hours is low due to the similarity of cloud tops and ice surfaces at IR wavelengths.

2.1.2. Sea ice concentration

The sea ice concentration (SIC) field uses the EUMETSAT OSISAF Global SIC CDR v2 product OSI-450 covering the period 1979–2015, and the OSI-430b the Interim CDR extension from 2016 onwards. The product is derived from coarse resolution (30-60 km) passive microwave (PMW) satellite data (SMMR, SSM/I and SSMIS). We hereafter label this whole time series as OSI-450, although the OSI-430b period is involved as well. In addition, we use data from the ESA CCI programme SICCI-25km product, which uses medium-resolution (15–25 km) PMW satellite data from AMSR-E (June 2002 to October 2011) and AMSR2 (July 2012 to May 2017). An extension of the SICCI-25km processing has been performed to provide consistent SIC fields after May 2017 using AMSR2 data. We hereafter label both the SICCI-25km and its extension as SICCI-25km. OSI-450 and SICCI-25km share the same algorithms, processing chains and data format (Lavergne et al., 2019), and continue earlier work by Andersen et al. (2007) and Tonboe et al. (2016). Both OSI-450 and SICCI-25km are presented at 25 km grid spacing. However, the true spatial resolution of OSI-450 is coarser due to the larger footprints of the SMMR, SSM/I and SSMIS channels used by the algorithm. The true spatial resolution of the SICCI-25km product is on the order of its grid spacing: 25 km. As other such SIC CDRs based on PMW satellite data, OSI-450 and SICCI-25km have challenges in coastal regions (Lavergne et al., 2019). For that reason, the SIC fields for the Baltic Sea consist of a SIC product based on ice charts from the Swedish Meteorological and Hydrological Institute (SMHI; 1982–2011) and the CMEMS 1 km SIC fields (2012-present), which include high resolution sea ice information from the Swedish and Finnish ice services. These Baltic Sea SIC products are similar to those used in the regional SST and IST CDR produced for the Baltic region (Høyer and Karagali, 2016).

2.1.3. Auxiliary data

An independent daily SST product has been used to filter the SIC product. SST from ESA SST CCI L4 Analysis CDR v2.1 is used from 1982 to 1990 (Good et al., 2019; Merchant et al., 2019), while the ESA SST CCI Analysis Long Term Product (Merchant et al., 2016) is used for the period 1991 to 2010, and the Operational Sea Surface Temperature and Sea Ice Analysis (OSTIA; Donlon et al., 2012; Good et al., 2020) is used from 2011 and onwards. These auxiliary products are obtained from the CMEMS catalogue (https://marine.copernicus.eu/) and they have a spatial resolution of 0.05° in latitude and longitude. The combined and independent SST product will be referred to as OSTIA/CCI in this paper. The OSTIA/CCI product is only included for filtering the SIC products and not as an input to the L4 SST generation.

2.2. In situ data

2.2.1. Sea surface temperature

For the SST validation, data from drifting buoys, moored buoys and Argo floats are obtained from the Hadley Centre Integrated Ocean

Database (HADIOD; Atkinson et al., 2014) version 1.2.0.0. The Argo and drifter observations are well represented in the Arctic region open waters, while the moorings are concentrated in the North Atlantic and Greenland Sea.

2.2.2. Ice surface temperature

For validation of IST, we use data from 116 drifting buoys obtained from the Meteorological Archival and Retrieval System (MARS) at the European Centre for Medium-Range Weather Forecasts (ECMWF) covering the period 1993–2015 (hereafter referred to as ECMWF buoys). These are supplemented with data from 96 U.S. Army Cold Regions Research Engineering Laboratory (CRREL) mass balance buoys for the period 2001–2017 (Perovich et al., 2016; Richter-Menge et al., 2006) as well as measurements from 14 Russian North Pole (NP) drifting ice stations mainly for the period 1982–1989 but also some for the period 2003–2012 (RU/FSR/HME/AARI and NSIDC, 1993). The temperature observations from NP, ECMWF and CRREL are air temperatures measured at different heights (typically around 2 m above the surface) depending on e.g. snow accumulation, snow drift and snow melt. These temperature observations have been inspected and quality controlled manually for data artefacts. The ECMWF and CRREL observations have previously been used for validation of satellite ISTs and corresponding 2 m air temperature estimates within the European Union's Horizon2020 project EUSTACE (EU Surface Temperatures for All Corners of Earth; Nielsen-Englyst et al., 2021; Rayner et al., 2020).

We also access 117 NASA IceBridge (IAKST1B) flights covering the period 2012–2019, typically conducted during March–May (version 2; Studinger, 2020). The surface temperatures are converted from IR radiation measurements from a Heitronics KT-19 IR Radiation Pyrometer by assuming an emissivity constant of 0.97. The surface temperatures are provided by IceBridge at a spatial resolution of about 15 m, and here they have been averaged for every fifth kilometer to remove the small scale variability, which cannot be represented by the coarser resolution L4 IST product.

3. DMIOI L4 processing system

This section presents the full DMIOI L4 processing system, which integrates individual, single sensor, swath based SST and IST observations to a multi-sensor interpolated (gap-free) field. The processing sequence is outlined in Fig. 2. The OI SIC field (derived and described in Section 3.a) is used as input to identify the different surface types (i.e. ocean, sea ice and the MIZ) for each day during the record. The surface is considered as open water when SIC≤15%, ice covered when SIC>70% and as MIZ when 15 < SIC≤70%. Together with the land mask the SIC is used to construct a dynamic surface mask. This dynamic surface mask is used during the pre-processing of the input L2 + L3 IST/SST to L3 Supercollated (L3S) data, which is described in detail in Section 3.b. The surface mask is also used during the derivation of the error statistics and covariances for each surface type, which are used in the OI method for analysis of the observations (see Section 3.c). In the end, the OI method produces the daily L4 SST/IST and the corresponding uncertainties. The L4 SST/IST generation and post-processing are described in Section 3.d.

3.1. Processing of OI Sea ice concentration

The OI SIC field (used as input for the DMIOI L4 Processing System) is based on different sources of sea ice information, which have been resampled onto the final L4 0.05° regular latitude longitude grid. As stated in Section 2.a.2), the SMHI/CMEMS products (Høyer and Karagali, 2016) are used within the Baltic Sea, while the SICCI-25km and OSI-450 SIC fields are used outside of the Baltic Sea. The SICCI-25km product is used whenever it is available and the OSI-450 product otherwise. The days with missing data are listed in the product user guides, and for these days the SIC field closest in time is used to construct a SIC record for all days from 1982 to May 2021. The SIC field has been extrapolated along the coasts to cover the fjords with SIC values. Low SIC (≤15%) is defined as no ice and the SIC is set to 0% in these grid cells.

Even though a land-spillover correction procedure is already applied in the SIC processing for SICCI-25 and OSI-450, erroneous ice is still common along ice-free coasts since the PMW brightness temperatures from ocean grid cells close to the coast often contain a mixture of the microwave emission from land and ocean (due to the large field of view). This land-spillover effect is more pronounced for the coarser resolution OSI-450 product than the SICCI-25km product (Kern et al., 2022; Lavergne et al., 2019). The resampling of the SIC products to the L4 0.05° grid results in oversampling of the coarse resolution SIC data, which also requires some filtering of the resampled SIC data to comply with the higher resolution SST data. To improve the resampled SIC fields (in particular the coarser resolution OSI-450) and to increase the consistency of the full SIC record, two filters have been used to minimize the effects from erroneous ice along the coasts. Both filters use a spatial 15 × 15 grid point filter around each 0.05° L4 grid cell. The first filter (F1) removes sea ice from the center grid cell if the group of 15 × 15 grid cells contains at least one land and one ocean grid cell. This approach is similar to the NOAA/NSIDC Bootstrap Land-Spillover Correction (Cho et al., 1996; Meier, 2012) for which the center grid cell is replaced by the minimum non-land value within the group of grid cells if at least one of the grid cells is land. The second filter (F2) removes sea ice from the

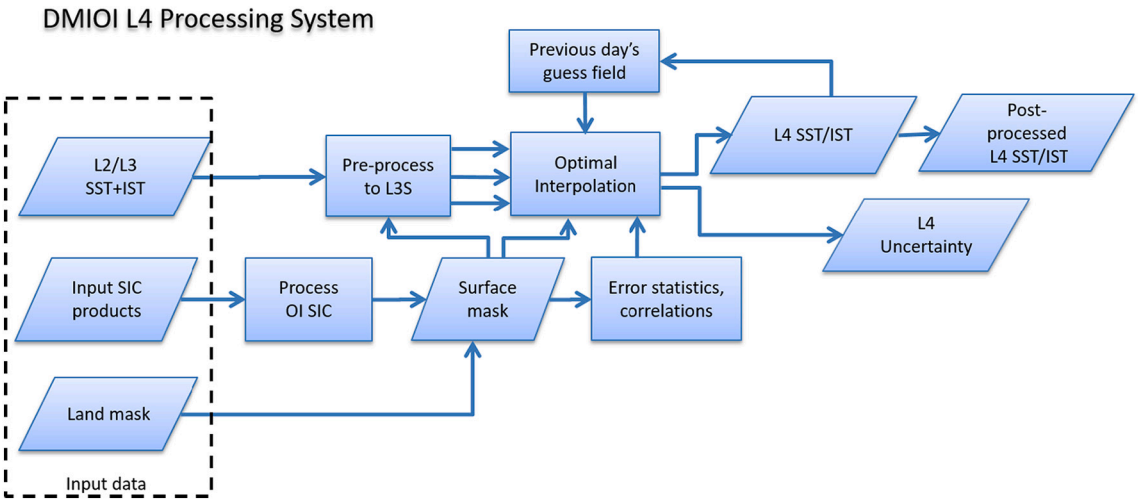

Fig. 2. Schematic diagram illustrating the processing steps of the DMIOI L4 Processing System.

center grid cell if any of the grid cells within the 15 × 15 group is land and the SST (from the OSTIA/CCI product) of the center grid cell at the same time exceeds 3 °C. The rationale for this is that the SST fields in general have fewer coastal issues as they are based on the higher resolution IR observations.

To examine the consistency between the different products, the resampled OSI-450 and SICCI-25km have been compared for 2018 with and without the filters. The Baltic Sea has been excluded in this comparison since the SMHI/CMEMS SIC products have been used here. In general, the largest differences between the resampled OSI-450 and resampled SICCI-25km are found along the coasts, where the resampled OSI-450 has numerous occurrences of sea ice grid cells, which are not seen in the resampled SICCI-25km. This is explained by the larger uncorrected land spill-over effects in OSI-450 compared to SICCI-25km.

Fig. 3 shows the distribution of sea ice as a function of SST (OSTIA/CCI) for OSI-450 and SICCI-25km during July 2018 in the case of no filter and both filters (F1 + F2) applied. July has been chosen as example month since it is one of the months with largest disagreement between OSI-450 and SICCI-25km as well as the month with most cases of coinciding sea ice and SST > 3 °C. As shown in Fig. 3a-b, OSI-450 has many cases of sea ice with SIC up to 60% in warm (6–15 °C) waters (before filtering) which are not seen in SICCI-25km. The OSI-450 and SICCI-25km agree much more after applying the two filters (F1 + F2), but with some remaining differences for warm SSTs (>10 °C).

A final filter (F3) has been applied to remove all sea ice in grid cells with OSTIA/CCI SST exceeding 8 °C. This SST threshold is more relaxed than what has previously been used (Hurrell et al., 2008; Markus and Cavalieri, 2009) and observed during in situ campaigns (Chiodi et al., 2021) to minimize the removal of true ice in regions with large SST gradients.

Before applying any filters, the resampled OSI-450 has more ice grid cells (SIC>15%) than the resampled SICCI-25km ranging from 0.88% more in March to 3.34% more in July. These ranges reduce to 0.84% in March and 2.84% in July after applying all filters (F1 + F2 + F3). The number of grid cells with SIC>15% and SST>3 °C is only a small fraction of all ice grid cells. Without any filters this fraction ranges from 0.018 to 0.639% and 0.002–0.162% for OSI-450 and SICCI-25km, respectively. After applying all the filters, these ranges are reduced to 0.002–0.197% and 0.000–0.140% for OSI-450 and SICCI-25km, respectively.

Fig. 4 provides detail of the number of ice grid cells with SST>3 °C for the entire SIC range (0<SIC≤100%) during July for the resampled OSI-450 and SICCI-25km in the cases where no filter, F1, or F1 + F2 + F3 has been applied. The filters remove limited sea ice in SICCI-25km compared to OSI-450. In OSI-450, F1 primarily removes sea ice with concentrations below 20% while adding F2 leads to removal of sea ice with SICs up to 80%. F3 removes very limited cases in comparison with F1 and F2. After filtering, the distribution of sea ice (with SST> 3°C) in OSI-450 looks more similar to the distribution in SICCI-25km.

The filtering method derived here removes many of the errors due to land spill-over, in particular in OSI-450, but some errors likely remain and likewise some true sea ice may be removed through the filtering. However, overall the filters have proven to be beneficial to reduce spurious ice and to reach higher consistency in the resulting combined and filtered SIC record (referred to as OI SIC). The preprocessed OI SIC

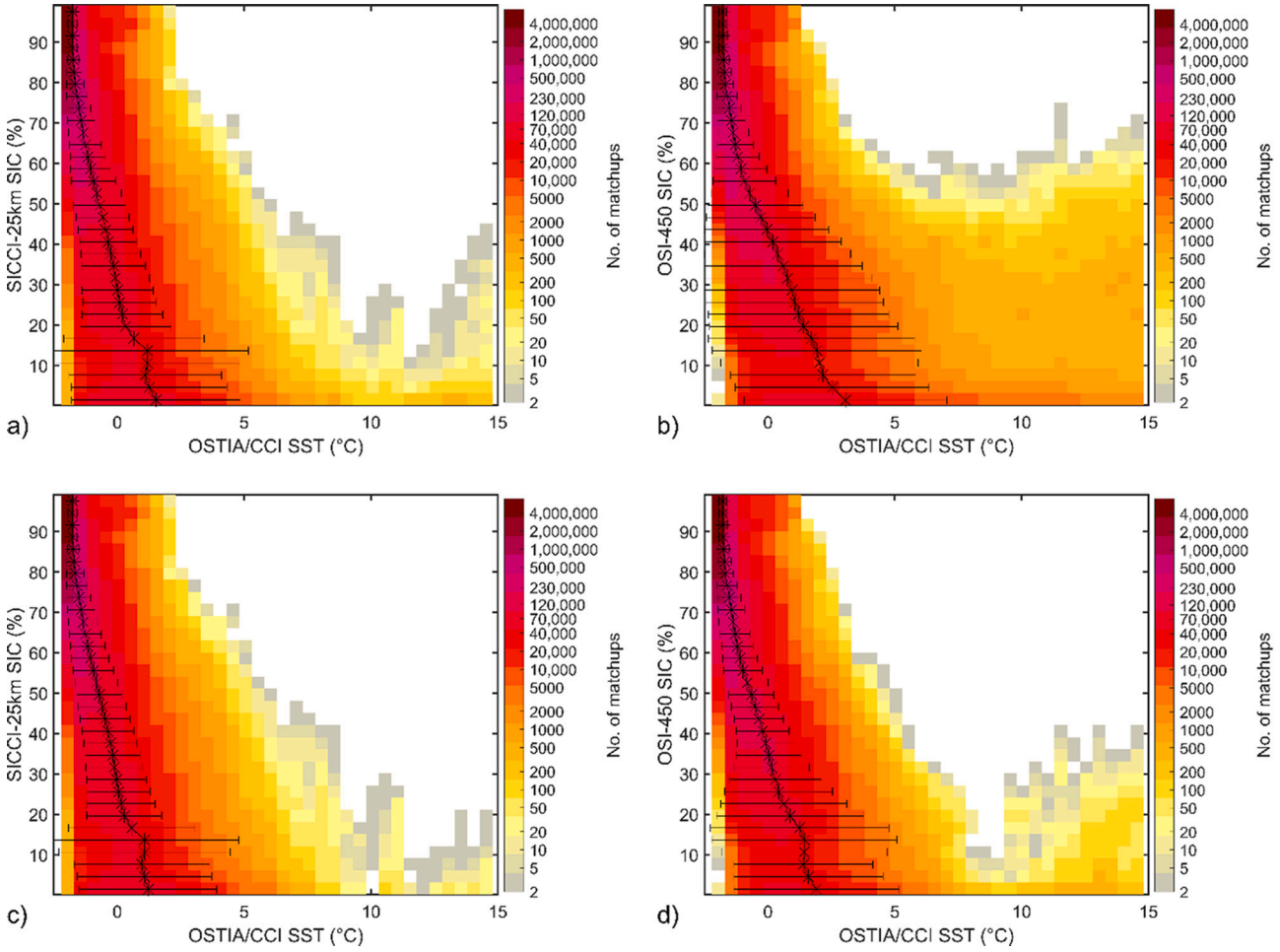

Fig. 3. OSTIA/CCI SST versus SIC from OSI-450 (right) and SICCI-25km (left) during July 2018 without filtering (top) and with both F1 and F2 filters applied (bottom). The average distribution is shown as asterisks with related error-bars showing the standard deviations considering bins with >30 members.

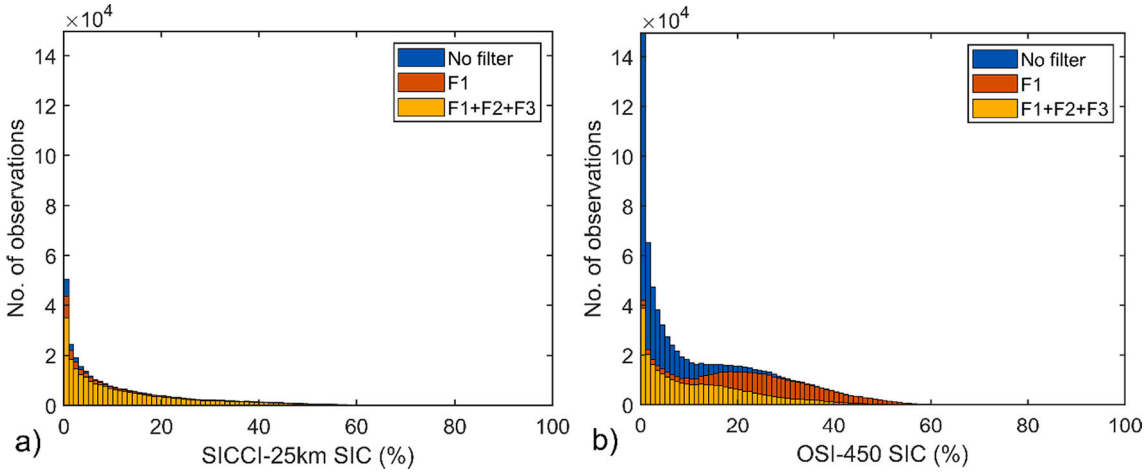

Fig. 4. The number of ice grid cells (SIC>0%) with SST>3 °C during July 2018 for a) SICCI-25km and b) OSI-450 in case where no filter, F1, or F1 + F2 + F3 filters have been applied, respectively.

field is used as input to the DMIOI L4 processing system for the L4 SST/IST generation (see Fig. 2).

3.2. Preprocessing of SST/IST satellite data

The input L2 SST and IST satellite data have been aggregated into L3S data by considering the available data within 24 h from the analysis. The L3S SST fields have been calculated as a noise weighted average of all available ATSR, AVHRR and SLSTR observations. Based on results from validation against in situ observations and the statistics from ingestion in the L4 analysis, we use the following uncertainties for ATSR, AVHRR, SLSTR and AASTI: 0.3 °C, 0.4 °C, 0.4 °C and 1.0 °C. AASTI ISTs are used over the MIZ and sea ice regions.

Only satellite data classified as cloud free by the cloud mask were included. Satellite observations processed using an IST algorithm in areas where the OI SIC field is zero were discarded. A minimum quality flag of 4 was used for all observations except from those from SLSTR, where a quality flag of 5 was required.

3.3. The optimal interpolation (OI) method

The aim of the OI method is to take an irregular distribution of observations, which may have different uncertainties and spatial resolutions, and provide the best possible estimate on a regular grid. This should be done by extracting the maximum information from all available observations and combining these using the proper weight of each observation. OI attempts to accomplish this by minimizing the mean-square interpolation error for a large ensemble of analysis situations. The OI method was first introduced by Gandin (1963) to produce gridded maps of meteorological variables, while oceanic applications was introduced by Bretherton et al. (1976) and has since then been widely used for mapping of SST (e.g. Høyer and She, 2007; Reynolds and Smith, 1994; White, 1995). The OI methodology used in this paper follows the high latitude SST DMI processing scheme (Høyer et al., 2014; Høyer and She, 2007). For the OI estimation, we assume that $\widehat{f}_i$ represents the ith observation of the field and can be written as

$$\widehat{f}_i = f_i + \varepsilon_i \tag{1}$$

where f_i is the true representative value of the field and ε_i is the observational error.

The construction of the OI field employs a first guess field, which in this case is provided as the analysis field from the previous day. The deviation of the estimated field from the first-guess field is calculated as a weighted sum of the nearby observed departures (anomalies) from the first guess:

$$f_0' = \sum_{i=1}^{n} (f_i' + \varepsilon_i) p_i + I_0, \tag{2}$$

where p_i are the weighting factors, I_0 is the interpolation error, n is the number of observations selected for the interpolation and the primes indicate anomalies from the first-guess field. Working with anomalies ensures that the first guess is preserved in regions with limited or no observations. It is assumed that the first guess is unbiased and that the noise on one observation is not correlated with the true value or with the noise of other observations (Bergman, 1978). The optimal weights should be chosen such that ε is minimized and this is obtained by differentiating ε partially with respect to each of the p_j and equate them to zero. By assuming that the variances are homogenous and the covariances are both homogenous and isotropic (i.e. only depending on the distance) the following set of linear equations can be derived:

$$\sum_{j=1}^{n} C_{i,j} p_j + \tau_i^2 p_i = C_{0,i}, \tag{3}$$

where p_i denotes the optimal weights, which need to be determined, $C_{i,j} = \frac{\overline{f_i' f_j'}}{\sigma^2}$ is the correlation function between the individual observations and $C_{0,i} = \frac{\overline{f_0' f_i'}}{\sigma^2}$ is the correlation function between the observations and the estimation point, and $\tau_i^2 = \frac{\sigma_{\varepsilon i}^2}{\sigma^2}$ with $\sigma_{\varepsilon i}^2$ being the error variance of the ith observation and σ^2 representing the variability. The OI method directly provides the mean-square interpolation error, which can be estimated in all grid points by

$$\varepsilon_{min} = \sigma^2 \left(1 - \sum_{i=1}^{n} C_{0,i} p_i\right). \tag{4}$$

From this, it follows that the mean-square interpolation error never exceeds the variance of the anomalies in the estimation point. Both the weights and the interpolation error depend on the scales of the correlations $C_{i,j}$ and $C_{0,i}$, on the variance, and on the random observational error, $\sigma_{\varepsilon,i}$. These are calculated prior to the prediction and assumed to be constant in time.

3.3.1. OI statistical parameters

The analysis field from the previous day is used as first guess and the corresponding first guess error variances are derived from a test run, where the L3 observations were compared against the previous day analysis and the standard deviations were calculated from the

anomalies. For IST, the first guess variance and error covariance have been derived using one year of Metop AVHRR L3 IST observations. For each day, the L4 field of previous day were subtracted from the L3 IST observations. The anomaly time series were then used to calculate the standard deviations for every grid point in order to obtain a spatial two dimensional field of standard deviations (Høyer et al., 2014). The first guess variance and error covariance for SST are the same as those used in Høyer et al. (2014), and Høyer and She (2007). In the MIZ (15% < SIC≤70%), the first guess variance and error covariance are calculated through a weighted linear combination of SST and IST values, using the OI SIC as a weighting factor.

Spatially varying correlation functions in the latitudinal and longitudinal directions have been derived empirically from the observations (i.e. one year (2018) of anomalies) by assuming steady state. For IST, L3 observations from METOP AVHRR were used, while L3 VIIRS observations (e.g. Liang and Ignatov, 2013) were used for SST due to the higher accuracy and higher spatial resolution (~750 m). The correlations are calculated by correlating time-series of anomalies within 10 × 10° bins. Separate functions were derived for open ocean, sea ice and the MIZ, due to the different variabilities in the temperature of the different surface types, but they share the same form:

$$C_{i,j} = exp\left(-\lambda \bullet dist_{i,j}^{\gamma}\right) \quad (7)$$

where $dist_{i,j}^{\gamma}$ is the distance between two observations, and λ and γ are the two empirically determined parameters that vary throughout the domain.

The true correlations will be larger than the observed correlation near zero lag because of the random noise in the observations. The difference in correlation resulting from the random noise (μ) has been estimated by measuring the drop in correlation from the estimation point (correlation = 1) to a small distance (2.5 km) for both IST and SST. Thereby, it is assumed that at distances smaller than 2.5 km from the estimation point, the drop in correlation can be fully attributed to the random noise. For the MIZ, the random noise has been estimated by assuming that the error of MIZT observations is equal to the error on IST observations. The estimated effect from the random noise has been removed before fitting the correlation functions. The fit results in 2D spatial fields of λ and γ for each of the three surface types. Fig. 5 shows the spatial 2D mean observed correlations including the random noise component for SST and IST using all available observations. They are calculated by correlating time-series of anomalies within 10 × 10° bins and ordering the results according to the distance in latitude and longitude.

Fig. 6 shows the best fit mean correlation models for SST, IST and MIZT in the latitudinal direction with the corresponding average values of λ and γ as listed in Table 1. The fitted mean correlations only include observations with >30 pairs of anomalies. The derived *e*-folding scales are shown in Table 1.

3.4. L4 SST/IST generation and post-processing

The derived OI statistical parameters have been used for the generation of the gap-free L4 SST/IST climate dataset. The correlations of all observations within the search radius (100 km) around the estimation point have been estimated and the observations used by the OI have been selected by taking the one with largest correlation within each quarter around the estimation point (if available). This has been repeated until the maximum number of observations (20) is reached or no more observations are available. On average, the selected number of observations used in the OI is 18.6, indicating good coverage. The coverage increases over time (with annual means ranging from 16.3 to 19.8) and reaches a maximum during winter (DJF) with a mean coverage of 19.1 and a minimum during summer (JJA) with a mean coverage of 17.6.

The interpolated anomalies have been added to the first guess field to provide the surface temperatures. Any anomalies exceeding ±9.9 °C

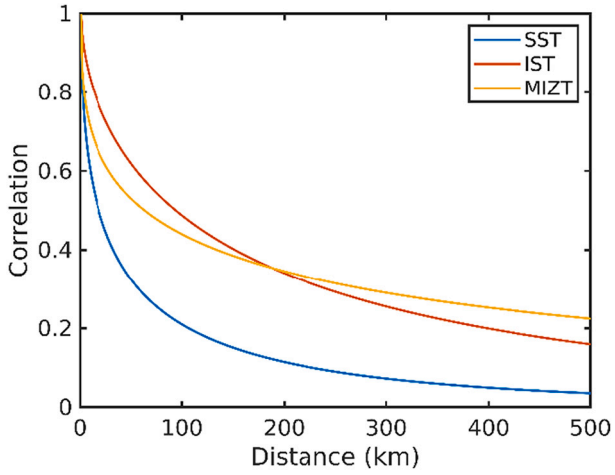

Fig. 6. The best fit mean spatial correlation in the latitudinal direction for SST, IST and MIZT.

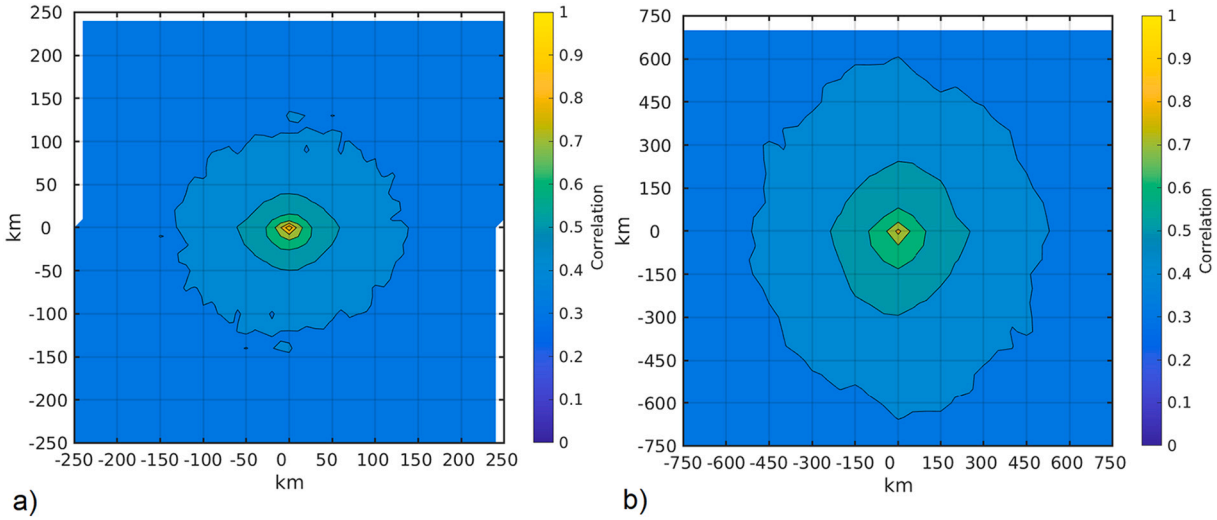

Fig. 5. Spatial mean of observed correlations (all 10 × 10° bins) for SST (left) and IST (right) with the estimated random noise added to the observations.

Table 1
The average covariance parameters, λ, γ, first guess error variance, σ^2, (°C), random noise, μ, and e-folding scale, e^{-1} (km) of each domain.

	SST (SIC≤15%)	IST (SIC>70%)	MIZT (15% < SIC≤70%)
λ	0.18	0.05	0.16
γ	0.47	0.58	0.37
σ^2	0.18	5.15	3.17
μ	0.24	0.29	0.47
e^{-1}	69.5	276.1	344.4

were reset to this value. Surface temperatures outside the accepted range (−60 to +35C°) have been reset to the closest of the two temperature limits.

The input satellite observations are all thermal IR observations which can only be utilized during clear-sky conditions. Here, the gaps due to clouds are filled using OI, but the aggregated and averaged daily surface temperatures are clear-sky averages, which may differ from the all-sky averaged surface temperature. For SST, the difference is small but over ice the clear-sky averaged IST is typically colder than the all-sky averaged IST (referred to as the clear-sky bias). Nielsen-Englyst et al. (2019) found an average cold clear-sky bias of 0.85 °C, using in situ observations over Arctic sea ice and a cloud mask derived from the

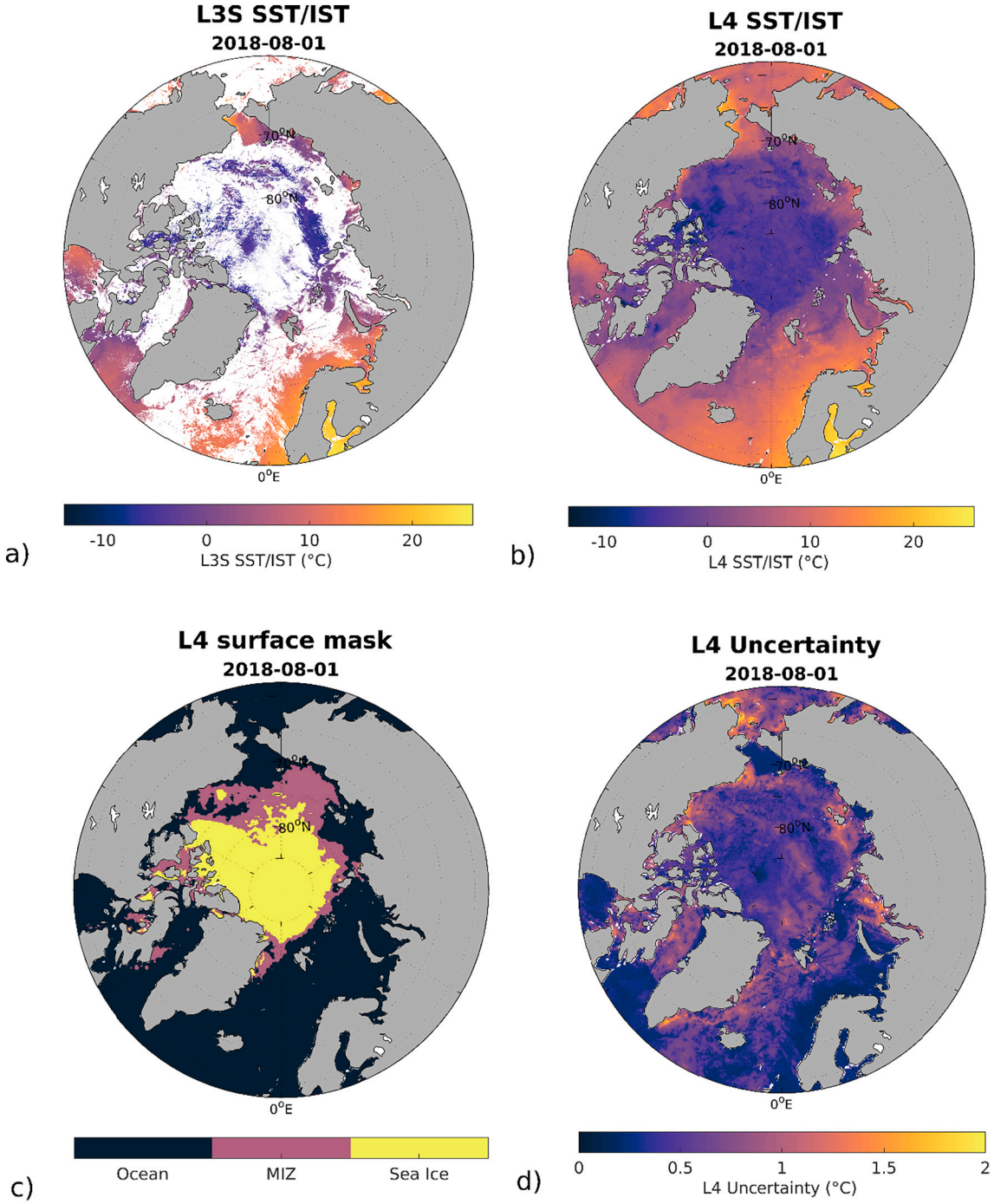

Fig. 7. An example of a) the combined L3S SST/IST field, b) the optimally interpolated L4 SST/IST field, c) the L4 surface mask, and d) the derived L4 uncertainty field for August 1, 2018.

longwave-equivalent cloud cover fraction. To minimize the clear-sky bias over ice in the L4 SST/IST product, we have introduced a constant bias correction over sea ice (SIC>70%) of +0.85 °C, which are linearly scaled towards 0 °C for open ocean using the SIC as a weighting factor.

No clear-sky bias correction has been applied to the SST in open water grid points (SIC≤15%), but a constant bias correction of 0.16 °C has been applied based on the validation against drifting buoys. It has been added to all open water grid points and the value is linearly scaled towards zero for 100% sea ice cover using the SIC as a weighting factor.

4. Results

The DMIOI L4 processing system has been used to generate a daily gap-free combined SST and IST reanalysis covering the Arctic (>58°N) with a spatial resolution of 0.05° for the period 1st of January 1982 to 31st of May 2021. An example of the combined SST and IST L3S field, the L4 SST/IST field, the L4 surface mask, and the L4 uncertainty field is shown in Fig. 7 for August 1, 2018.

4.1. Validation

The L4 SST and IST fields have been validated separately using the independent in situ observations listed in Section 2.b. The OI SIC field is only used as a mask for ocean/ice identification, and it will not be validated. Table 2 shows the overall validation statistics against independent in situ observations for SST and IST. The statistics are divided into the different sources of in situ observations due to differences in type and error characteristics. For both SST and IST, matchups with L4 – in situ temperature differences deviating more than three times the standard deviation (i.e. 3σ) from the mean L4 – in situ temperature difference have been excluded. This has been done for the individual observation types to avoid effects from outliers. The results of the SST and IST validation are discussed separately in the two following sections.

4.1.1. Sea surface temperature

The L4 SST (SIC≤15%) have been validated against drifting buoys, moored buoys, and Argo floats. Matchups with in situ SST or L4 SST colder than −1.8 °C have been excluded from the validation statistics. Table 2 shows that the L4 SST have mean differences <0.05 °C and standard deviations <0.6 °C, and correlations above 0.98 when compared against drifting buoys, moored buoys, and Argo floats. The Argo floats and moored buoys provide independent validation statistics while the drifting buoys have been used to adjust the L4 SST (see Section 3.d). The mean differences are lower than those reported by Castro et al. (2016) where nine different SST analyses and two single sensor satellite products were compared with independent observations from Upper Temperature of the polar Oceans (UpTempO) buoys deployed in the Beaufort Sea in 2012 and 2013. The standard deviations reported here are slightly lower than in Castro et al. (2016) for most cases, but higher than those reported for the most northern UpTempO buoys where SSTs were very uniform and lower than for those observations that coincided with a summer storm over the Arctic Ocean.

Table 2
Overall validation statistics of the L4 SST and IST against in situ observations. The mean difference is given by L4 SST/IST minus in situ SST/IST. Notice that the NP, ECMWF and CRREL do not measure the surface temperature, but the air temperature (T2m). For both the SST and IST validation a 3σ filter has been applied before calculating the statistics. The table shows the mean difference (MD), standard deviation of the difference (std), root mean squared error (RMSE), correlation (corr) and the number of observations (Nobs).

Type	Parameter	MD	std	RMSE	corr	Nobs
Drifting buoys	SST (°C)	0.00	0.54	0.54	0.99	3,062,549
Moored buoys	SST (°C)	0.03	0.56	0.56	0.98	76,052
Argo	SST (°C)	0.03	0.51	0.51	0.99	32,953
NP drifting ice stations (T2m)	IST (°C)	−2.35	3.12	3.91	0.98	7665
Drifting buoys ECMWF (T2m)	IST (°C)	−3.21	3.34	4.63	0.96	55,288
Drifting buoys CRREL (T2m)	IST (°C)	−2.87	3.36	4.42	0.96	22,979
IceBridge KT-19 (IST)	IST (°C)	1.52	3.12	3.48	0.92	36,638

Fig. 8 shows the seasonal (3-month) mean L4 SST differences (L4 SST – in situ SST) and standard deviations for the period 1982–2021, when compared to drifting buoys, moored buoys, and Argo Floats. It should be noted that the amount of drifting and moored buoys are much lower in the beginning of the time period compared to the latest years, which makes the validation statistics against drifter and moorings less reliable in the beginning of the record. The Argo floats are only available from May 2001. The statistics are only calculated for 3-month periods with >45 matchups available. Overall, the mean difference and standard deviation are both quite stable over the period of time for all three types of in situ observations. The combined trend in the mean difference is plotted (Fig. 8) and the corresponding overall trend is −0.0002 °C/yr indicating a very stable performance. The trends for the individual in situ types are −0.0001 °C/yr, −0.0019 °C/yr and 0.0027 °C/yr for drifters, moorings and Argo floats, respectively.

4.1.2. Ice surface temperature

The validation of the L4 IST (SIC>15%) is limited by the sparse number of in situ observations as well as increased in situ uncertainties in the ice covered regions compared to the open ocean. The L4 IST is colder than in situ measurements from NP, ECMWF and CRREL, while the L4 IST is warmer than KT-19 measurements from IceBridge flights. NP, ECMWF and CRREL do not provide the surface temperature, but the air temperatures measured at a varying height, typically of about 2 m (T2m). Nielsen-Englyst et al. (2019) found an average IST-T2m difference of −1.25 °C during all-sky conditions over sea ice. This IST-T2m difference is a real temperature difference between the snow surface and the air above it. This explains part of the temperature differences observed in the validation results against NP, ECMWF and CRREL (presented in Table 2), which is not related to the performance of the L4 IST. In Section 5, this topic is further discussed. Fig. 9 shows the seasonal mean L4 IST difference and standard deviation against NP, ECMWF and CRREL observations, respectively. The statistics are only calculated for the 3-month periods with >45 matchups available. The combined trend in the mean difference is −0.0166 °C/yr, while the individual trends are 0.0047 °C/yr, −0.0391 °C/yr, and 0.0676 °C/yr for NP, ECMWF buoys and CRREL buoys, respectively. A seasonal cycle is present both in the mean difference and the standard deviation. The larger standard deviations during winter are explained mainly by the larger temperature variability during winter, but also by the higher uncertainties in the cloud masking during winter (Nielsen-Englyst et al., 2019). The seasonal variation in the mean difference is corresponding to what was observed in the L3 IST validation and in Nielsen-Englyst et al. (2021).

The L4 IST validation against IceBridge includes 117 IceBridge flights, which provide measured surface temperatures in the period 2012–2019. The IceBridge data are smoothed for every fifth kilometer if >30 observation points were available. Fig. 10 shows an example of the validation against one single IceBridge flight from March 2012. Despite the smoothing of the data, there are still large fluctuations in the IST measured by IceBridge, which are not captured by the L4 IST. These are results of warm leads (open or newly refrozen) in the sea ice and some of the largest ones are actually captured to some extent by the L4 IST. Overall, the figure shows a quite good agreement between IceBridge and the L4 IST in this particular example, with a mean difference of 1.24 °C and a standard deviation of 1.11 °C. Considering all 117 IceBridge flights, and weighting all observations equally, the IST validation shows a mean difference of 1.52 °C, standard deviation of 3.12 °C and correlation of 0.92 (see Table 2) using the 3σ filter on the differences. The

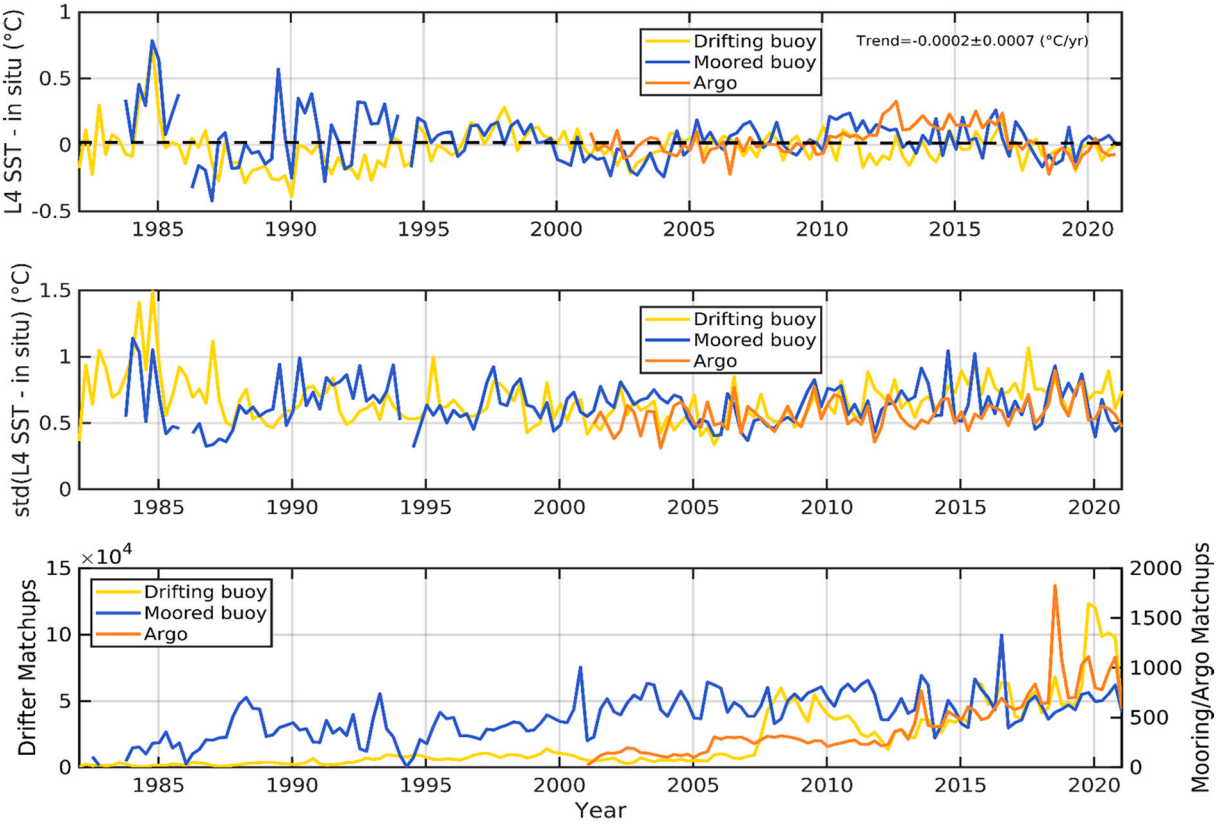

Fig. 8. Seasonal (3-month) mean L4 SST difference (top) and standard deviation (middle) against sea surface temperatures measured by drifting buoys, moored buoys and Argo floats. The bottom plot shows the seasonal mean number of matchups for each in situ source. The linear trend in the mean difference is calculated considering all in situ types. The seasonal difference, standard deviation and trend are only calculated if >45 matchups are available.

IceBridge observations have standard deviations of the 5 km averages ranging from 0.81 °C to 5.41 °C for the different flights and an average value of 2.52 °C. Part of the bias against IceBridge may be explained by the missing cloud screening of IceBridge observations. If clouds are present between the flight and the surface, the radiometer will provide the temperature of the (usually colder) clouds instead of the surface temperature. Furthermore, IceBridge provides "snap-shots" of the surface temperature, while the L4 SST/IST provides daily means, which have been adjusted by using the 24 h average clear-sky bias correction (see Section 3.d).

4.1.3. Uncertainties

Each daily L4 SST/IST is accompanied with an uncertainty estimate, which is a direct output of the OI method (see Eq. 4). The uncertainties for the L4 SST have been validated against drifters. The validation results are shown in Fig. 11, where the actual L4 SST minus drifter SST differences are plotted as a function of the OI derived uncertainty estimates. This uncertainty validation approach is similar to what is done in Alerskans et al. (2020) and Nielsen-Englyst et al. (2018). The dashed lines represent the ideal uncertainty based on the assumption that drifters have a total uncertainty of 0.2 K (Kennedy, 2014). The figure shows a good agreement between the estimated uncertainties and the L4 SST uncertainties for low uncertainties, but overestimated uncertainties for the higher uncertainties. This approach is unfortunately not applicable for the IST validation results due to the lack of good quality in situ reference observations that makes the spatial sampling component very large in comparisons between the L4 IST and the in situ measured near surface air temperatures.

4.2. Climate analysis

The derived L4 SST/IST product is the first gap-free combined SST and IST reanalysis product for the Arctic. The combination of sea ice and ocean surface temperatures in the Arctic provides a consistent climate indicator, which can be used to monitor day-to-day variations as well as long-term climate trends. Fig. 12 shows the average seasonal variation of the daily surface temperature and the sea ice to open water ratio of the Arctic (>58°N). The daily surface temperature reaches a maximum in August with average surface temperature around the melting point and minimum temperatures in February/March with average temperatures around −24 °C. During the minimum in September, only 30% of the L4 SST/IST region is covered with sea ice (and 70% open ocean), while the fraction increases to almost 70% during winter (30% for open ocean). The largest variability in temperature is seen during winter. Part of this is explained by stronger cyclones and anticyclones in contrast to the summer (Serreze et al., 1993), when the variability moreover is limited by the upper temperature limit around the melting point for the ice covered regions. For regions covered by seasonal sea ice, the SSTs usually also stay around the melting point during summer, when the sea ice has retreated(e.g. Timmermans and Labe, 2020), limiting the summer SST variability in these regions as well. The large variability in winter temperatures as well as in the sea ice coverage, shown in Fig. 12, is also explained by the increasing temperatures and decreasing sea ice extent throughout the data record (1982–2021).

Fig. 13 shows the monthly mean surface temperature anomaly for the period 1982–2021 when compared against the monthly mean of the 30-year-long reference period, 1991–2020. The large fluctuations illustrate large monthly variations in sea and ice surface temperatures of the Arctic. The solid black curve represents the yearly mean and the dashed black curve is the linear fit. During the period from 1982 to 2021

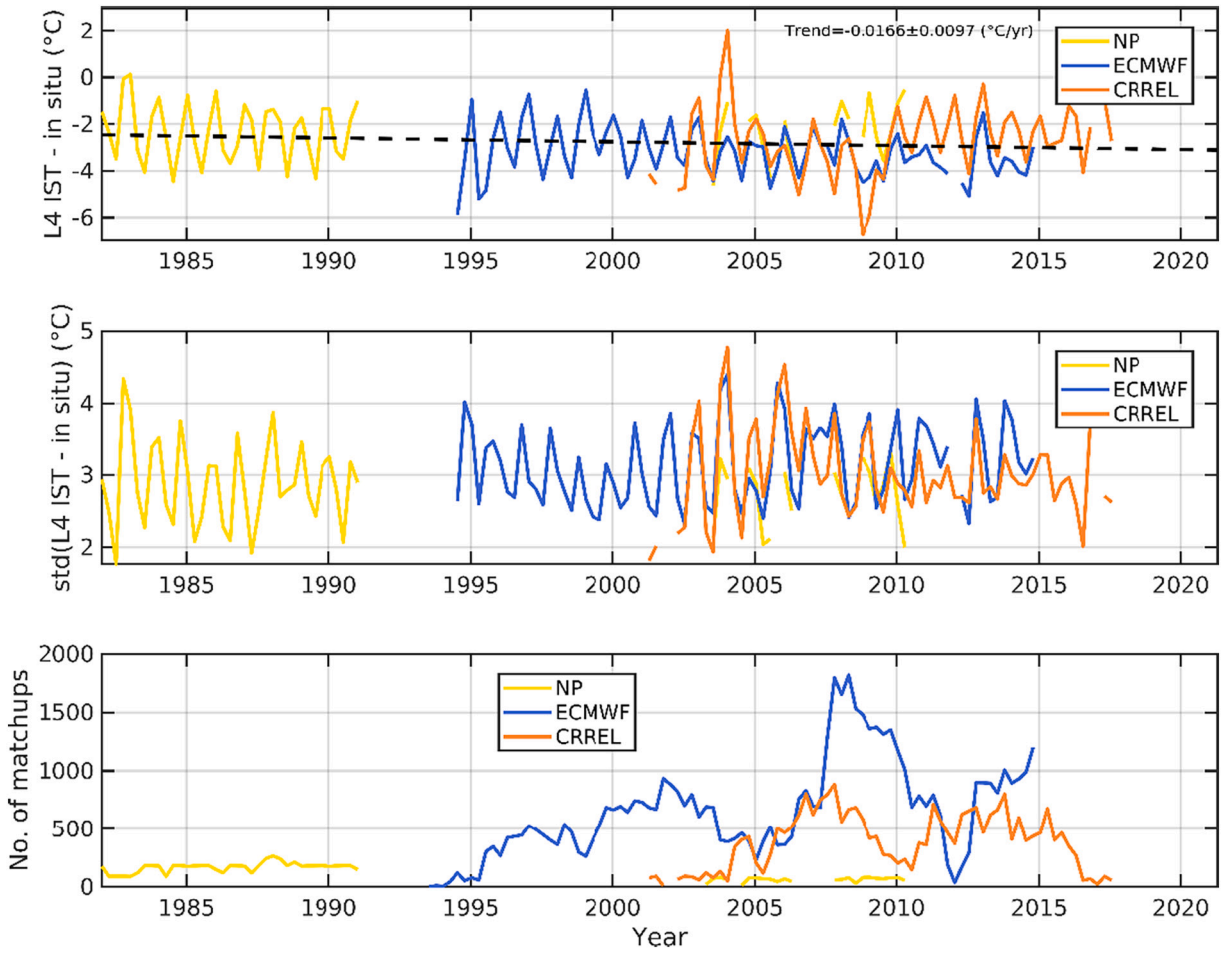

Fig. 9. Seasonal (3-monthly) mean L4 IST difference (top) and standard deviations (middle) against air temperatures from NP, ECMWF, CRREL. The bottom panel shows the seasonal mean number of matchups for each in situ type. The linear trend in the mean difference is calculated considering all in situ types. The seasonal mean difference, standard deviation and trend are only calculated if >45 matchups are available.

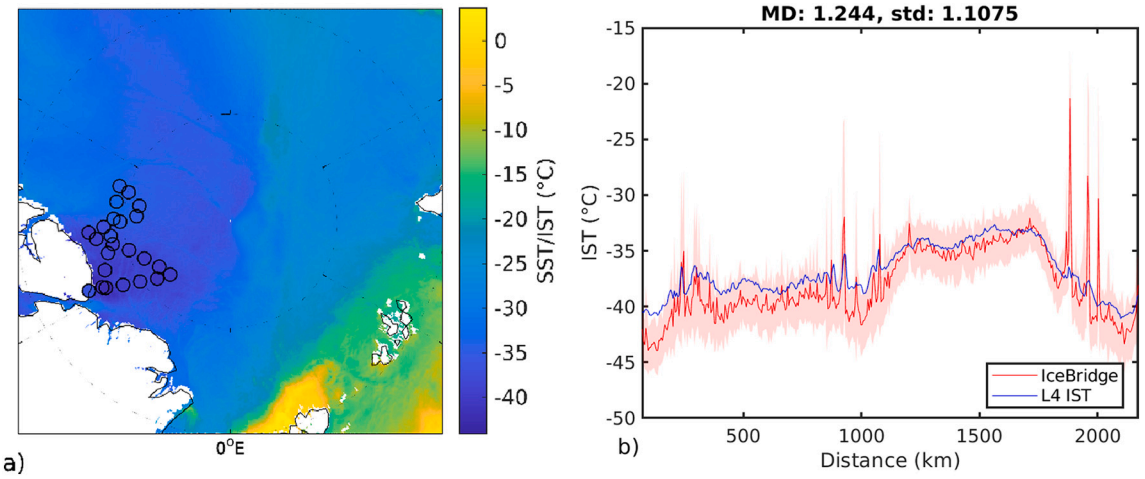

Fig. 10. An example of the validation against one Icebridge flight during March 29, 2012. Figure a) shows the flight path, while b) shows a comparison of the smoothened IceBridge IST and the L4 IST, with a mean temperature difference of 1.24 °C and a standard deviation of 1.11 °C.

the linear trend is 0.114 °C/yr, and the surface temperatures of the Arctic Ocean (>58°N) have thus increased by about 4.5 °C in 39 years. The trend increases with latitude and the total temperature increase to about 5 °C north of 70°N. Fig. 14 shows the corresponding two dimensional trend in the monthly Arctic surface temperatures for the entire period, 1982–2021. On average, the temperature has increased in most regions, with the largest increase in the northeastern Barents Sea, which shows a peak temperature increase of about 10 °C over the 1982–2021 period. The trend pattern is in agreement with the most recent findings based on combined observed and modelled data over the Arctic Ocean

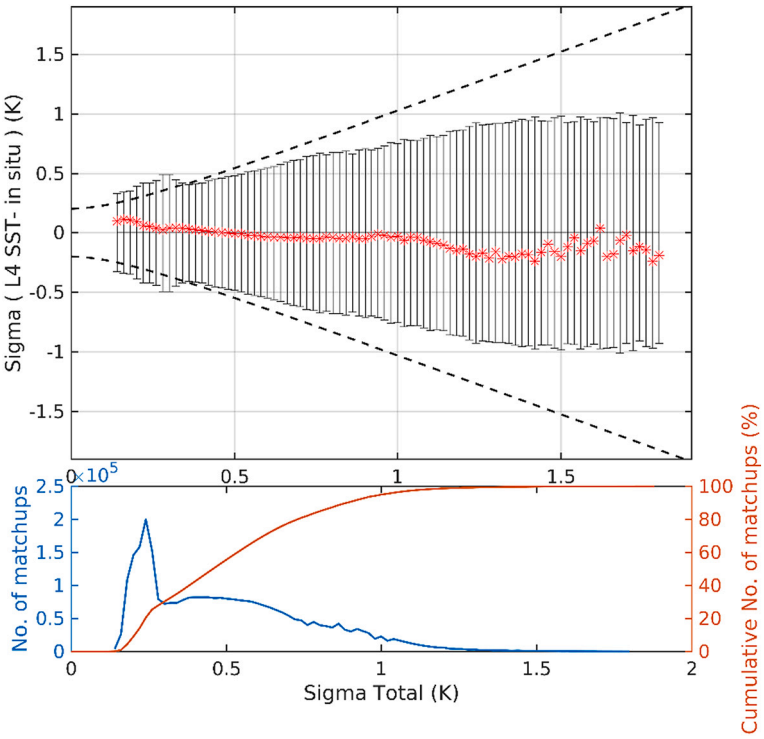

Fig. 11. L4 SST uncertainty validation against independent in situ observations from drifters. The dashed lines show the ideal uncertainty when accounting for uncertainties in the drifter SSTs and the sampling error. The solid black lines show one standard deviation of the L4 SST minus drifter SST differences for each 0.02 K bin and the red asterisks mark the mean difference. The bottom plots show the number of matchups (blue) and the cumulative percentage of matchups for each bin (red). (For interpretation of the references to colour in this figure legend, the reader is referred to the web version of this article.)

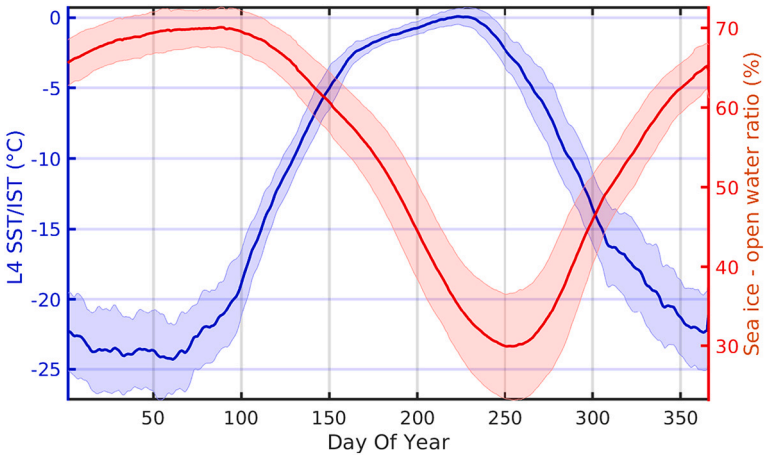

Fig. 12. Seasonal cycle of daily mean L4 SST/IST (blue) and daily mean sea ice – open water ratio in percentage of the total L4 SST/IST coverage (red) considering all years, 1982–2021. The shaded regions show one standard deviation. (For interpretation of the references to colour in this figure legend, the reader is referred to the web version of this article.)

for the period 1979–2019 (AMAP, 2021) and a combination of four observational datasets covering the period 1979–2021 (Rantanen et al., 2022). The largest temperature increases are coinciding with those regions where the number of open water days have increased the most (Tonboe et al., 2016). In general, the surface temperature increases observed in Fig. 14 are slightly larger than the air temperature increases observed in AMAP (2021) and (Rantanen et al., 2022), who find maximum temperature increases of around 6–8 °C in the northeastern Barents Sea. The largest surface temperature trends are found during fall (September–November) and winter (December–February) with average trends of 0.148 °C/yr and 0.142 °C/yr, respectively, leading to an average temperature increase of >5.5 °C from 1982 to 2021 considering these months. During summer (June–August), limited increase in the surface temperature (0.037 °C/yr) is observed. The small trend during summer is mainly explained by the upper constrain of the sea ice surface temperature to the melting point and the fact that the SSTs usually stay around the melting point during summer in regions where the seasonal sea ice has retreated (e.g. Timmermans and Labe, 2020).

5. Discussion

In order for a dataset to be categorized as a CDR it needs to have sufficient length, accuracy and stability to enable study and assessment of long-term climate variability and change (Minnett et al., 2020). A dataset with excellent absolute accuracy is important for understanding climate processes, but not necessary for determining long-term changes or trends as long as the dataset has the required stability (Ohring et al., 2005). Based on the expected magnitude of a climate change signal (per decade), the requirements of an SST CDR are an accuracy of 0.1 °C and a stability (per decade) of 0.04 °C according to Ohring et al. (2005). The

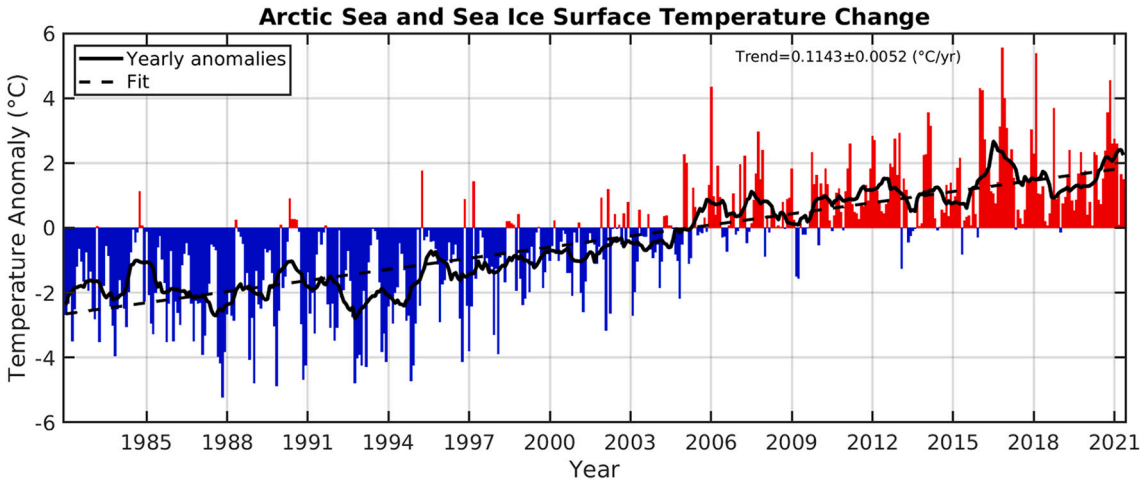

Fig. 13. Monthly mean surface temperature anomalies for the period 1982–2021. The anomalies represent the difference between the monthly mean surface temperature and the monthly mean surface temperature of the reference period, 1991–2020. The yearly mean anomalies are shown as the solid black curve, while the dashed black curve is the linear fit, which has a slope of 0.114 °C/yr.

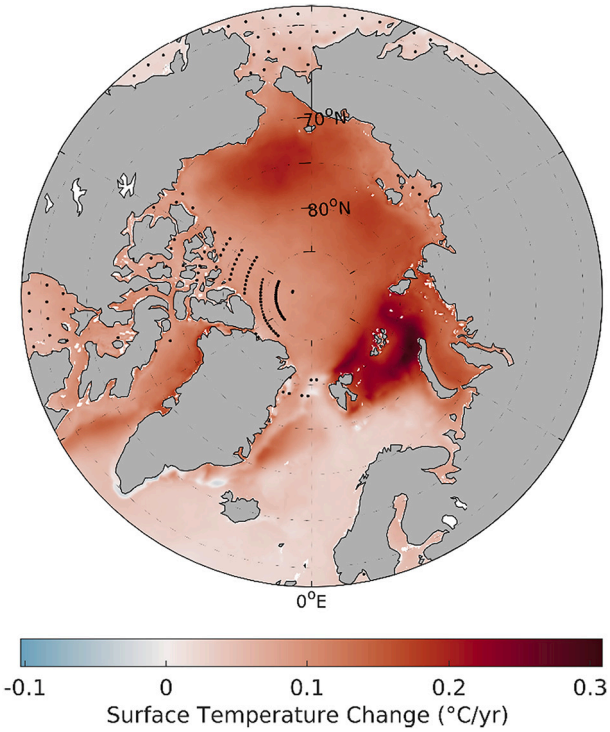

Fig. 14. The average rate of surface temperature change (°C) per year based on the monthly mean L4 SST/IST from January 1, 1982 to May 31, 2021. The black dots indicate regions where trends are not significant.

observed accuracy and stability of the L4 SST meet these SST CDR requirements. For land surface temperature (LST), including land surfaces covered with snow and ice, the CDR requirements are 0.3 °C/decade for the threshold stability and 0.1 °C/decade for the target stability (GCOS, 2016). The L4 IST meets the target requirements when considering the NP validation (which spans the longest time period). Currently, no GCOS requirements have been established for sea ice surface temperature, because this variable is not recognized as an Essential Climate Variable (ECV). Introducing IST as an official GCOS ECV is highly recommended in order to facilitate a common community consensus on IST requirements for climate applications (Lavergne et al., 2022). Moreover, the limited availability of long-term high quality reference in situ IST observations (with known and controlled stability), complicates validation and hence, the extent to which satellite IST products can be tested for meeting the CDR requirements.

In CDRs, quantitative uncertainty information should also be provided with the observations (Merchant et al., 2017). Here, each daily L4 SST/IST is accompanied with an uncertainty estimate derived directly from the OI method. The validation of the L4 SST uncertainty estimates (see Section 4.a.3) shows that the OI method is capable of deriving reliable uncertainty estimates for SST.

The validation of the L4 SST shows differences smaller than 0.05 °C and standard deviations <0.6 °C against drifters, moorings and Argo floats. The L4 IST is colder than in situ measurements from NP, ECMWF and CRREL, and warmer than KT-19 measurements from IceBridge flights with an average difference of 1.52 °C. The L4 IST differences were in the range from −3.21 °C to −2.35 °C and standard deviations of about 3.4 °C against T2m measurements from NP, ECMWF and CRREL. A large fraction of these differences can be attributed to the temperature difference between the in situ air temperatures measured about 2 m height and the actual surface temperature provided by the L4 IST product. Nielsen-Englyst et al. (2021) derived a simple regression model to convert satellite observed ISTs to 2 m air temperatures (T2m) over ice surfaces. Using the sea ice regression model and coefficients from Nielsen-Englyst et al. (2021) to derive T2m from the L4 ISTs, the absolute differences against CRREL, ECMWF and NP reduce to below 0.7 °C, while the standard deviations remain more or less the same. These initial results indicate that it is possible to derive reliable T2m above the sea ice on basis of satellite derived L4 ISTs in order to supplement the sparse in situ air temperature network in the Arctic.

Traditionally, gridded and gap-free satellite SST products provide the temperature of the sea water just below the ice in ice covered regions and this is also the case for the OSTIA/CCI and the NOAA Optimum Interpolation SST (OI SST v2; Reynolds et al., 2007, 2002), which are used in the comparison here. The NOAA OI SST v2 shows an overall warming trend in the Arctic Ocean (>65°N) of 0.036 ± 0.03 °C/yr considering the period from 1982 to 2018 (Carvalho and Wang, 2020), while a trend of 0.015 ± 0.003 °C/yr is found using OSTIA/CCI for the same region and time period. Considering the L4 SST/IST region (>58°N) and period (1982–2021), OSTIA shows an overall warming trend of 0.016 ± 0.001 °C/yr. To enable a comparison against the L4 product derived here, the OSTIA SST has been compared with the L4 SST product for regions that never experience sea ice (considering both products). The two products show very similar spatial trend fields, and the average trend is 0.019 °C/yr for OSTIA and 0.022 °C/yr for the L4 SST product, indicating a good agreement in those regions where both

products always report the temperature of the ocean surface.

In ice covered regions, limited variation is seen in the sub-ice SSTs, and this is not representative for the actual surface conditions. Instead, T2m is normally used in global reanalyses in ice covered regions in combination with SST over the ocean (Dee et al., 2011; Hersbach et al., 2020; Kobayashi et al., 2015; Simmons, 2004). A combination of modelled and observed data for a 49-year long period (1971–2019) showed an average increase in annual near-surface air temperature of 0.063 °C/yr (AMAP, 2021). Marquardt Collow et al. (2020) compared 12 reanalyses of the central Arctic Ocean and found an average trend in SST/T2m of 0.09 ± 0.01 °C/yr for the period 1979–2017 with large spread among the reanalyses (estimated standard deviation of the regression coefficient of 0.2 K). Using the derived T2m estimates from the L4 IST (following Nielsen-Englyst et al., 2021) together with our L4 SST, the combined SST/T2m trend in the Arctic is 0.100 ± 0.005 °C/yr for the region above 58°N and 0.111 ± 0.006 °C/yr above 70°N. This is in good agreement with the average estimate of the 12 reanalyses in the central Arctic Ocean.

Currently, global reanalyses only assimilate in situ measured air temperatures over ice. As a consequence, the global reanalyses usually show large uncertainties and significant differences in the Arctic due to the limited number of in situ observations in this region (Cowtan and Way, 2014; Lenssen et al., 2019; Marquardt Collow et al., 2020; Rapaić et al., 2015). Marquardt Collow et al. (2020) concludes that more in situ and remote sensing observations as well as a better use of existing satellite observations are needed in order to represent the characteristics of the entire Arctic region in both reanalyses and numerical models. Therefore, the L4 SST/IST product as well as a satellite derived T2m dataset based on the L4 IST product have a large potential to supplement existing in situ measurements and improve the current surface air temperature estimates over the Arctic sea ice (Nielsen-Englyst et al., 2021). The L4 SST/IST product has been derived for the Arctic, and the same procedures can be applied to the Antarctic.

Future work should aim at improving the L4 SST/IST product. One possible way of improving the L4 IST could be to include other available IST satellite products such as the MODIS IST data (Hall et al., 2004) or the VIIRS IST product (Key et al., 2013; Liu et al., 2015). More and higher quality in situ observations will also increase the possibilities of improving the satellite derived IST products and also allowing a better parameterization of the constant clear-sky bias, which is believed to have a seasonal variation. In general, there is a need for good quality reference data over sea ice, and in particular observations that also cover the MIZ, to improve retrieval derivation and validation.

In relation to SST, inclusion of other SST products may lead to improvements e.g. those based on PMW observations. The IR observations used as input to the L4 SST/IST product are severely limited by clouds, which are particularly extensive over the Arctic during summer (Intrieri, 2002; Key, 1990). PMW SST observations may provide an important supplement to the IR observations, since they are not prevented by non-precipitating clouds (Chelton and Wentz, 2005; Wentz et al., 2000). A number of different retrieval algorithms have been developed to retrieve SST from PMW observations (Alerskans et al., 2022, 2020; Chang et al., 2015; Meissner and Wentz, 2012; Milman and Wilheit, 1985; Nielsen-Englyst et al., 2018; Shibata, 2006; Wentz and Meissner, 2000). Hence, future work should investigate the possibilities of including PMW SST observations in the L4 SST/IST product derived here. This is particular of interest since the Copernicus Imaging Microwave Radiometer (CIMR), currently being implemented by ESA as a Copernicus Expansion Mission, will provide high-accuracy, high resolution PMW observations of the Polar Regions, which can be used to improve SST and SIC products in the future (Donlon, 2020).

6. Conclusion

This paper presents the first gap-free (L4) surface temperature climate dataset covering the ocean, sea ice and the marginal ice zone (MIZ) of the Arctic (>58°N) for the period from 1982 to May 2021. The dataset is based on thermal infrared observations from A(*A*)TSR, AVHRR and SLSTR, which have been combined using optimal interpolation (OI). Due to differences in the variability over ice, ocean and the MIZ, the OI statistical parameters have been derived separately for each surface type.

The derived L4 sea surface temperature (SST) and sea ice surface temperature (IST) product has been compared with different sources of in situ observations. The validation of the L4 SSTs shows mean differences of 0.01 °C, 0.04 °C and 0.04 °C and standard deviations of 0.54 °C, 0.56 °C and 0.51 °C for drifting buoys, moored buoys and Argo floats, respectively. The L4 ISTs have been compared with KT-19 measurements from 117 IceBridge flights, showing a mean difference of 1.52 °C and standard deviation of 3.12 °C, and with air temperatures (typically measured at about 2 m height) from the North Pole (NP) ice drifting stations as well as ECMWF distributed buoys and CRREL buoys, with mean differences of −2.35 °C, −3.21 °C and –2.87 °C and standard deviations of 3.12 °C, 3.34 °C and 3.36 °C, respectively. The large temperature differences against NP, ECMWF and CRREL are linked to the physical temperature difference between the skin ISTs provided here and the air temperatures measured in situ. The observed stability is −0.0001 °C/yr and 0.0047 °C/yr against drifters (SST) and NP (IST) observations, respectively, indicating a very stable performance throughout the record.

Traditionally, climate surface temperature trends have been estimated individually for SST and IST satellite based records. This is problematic in the Arctic region due to the large variability in the sea ice cover on decadal timescales, and the resulting climate trends are not easy to interpret. A combined surface temperature dataset of the ocean, sea ice and the MIZ provides a consistent climate indicator, which is important for monitoring day-to-day variations as well as climate trends in the Arctic region. The combined sea and sea ice surface temperatures of the Arctic have increased by around 4.5 °C between 1982 and 2021, with a peak warming of around 10 °C in the northeastern Barents Sea.

Data availability statement

The L4 SST/IST data are released through the Copernicus Marine Service, product SEAICE_ARC_PHY_CLIMATE_L4_MY_011_016 (doi: https://doi.org/10.48670/moi-00123) and will be updated regularly. For more information, see https://resources.marine.copernicus.eu/product-detail/SEAICE_ARC_PHY_CLIMATE_L4_MY_011_016/INFORMATION.

CRediT authorship contribution statement

Pia Nielsen-Englyst: Conceptualization, Methodology, Software, Investigation, Writing – original draft, Writing – review & editing. **Jacob L. Høyer:** Conceptualization, Methodology, Software, Investigation, Supervision, Writing – original draft, Writing – review & editing. **Wiebke M. Kolbe:** Methodology, Software, Investigation, Writing – original draft. **Gorm Dybkjær:** Investigation, Software, Writing – original draft. **Thomas Lavergne:** Software, Writing – original draft. **Rasmus Tage Tonboe:** Supervision, Writing – original draft. **Sotirios Skarpalezos:** Software. **Ioanna Karagali:** Project administration, Writing – original draft.

Declaration of Competing Interest

The authors declare that they have no known competing financial interests or personal relationships that could have appeared to influence the work reported in this paper.

Data availability

Data will be made available on request.

Acknowledgments

This work is funded by the Copernicus Marine Environment Monitoring Service (CMEMS) and the Danish National Centre for Climate Research (NCKF) at the Danish Meteorological Institute (DMI). The authors would like to thank Leif Toudal Pedersen for his valuable inputs and constructive feedback during this work.

References

Alerskans, E., Høyer, J.L., Gentemann, C.L., Pedersen, L.T., Nielsen-Englyst, P., Donlon, C., 2020. Construction of a climate data record of sea surface temperature from passive microwave measurements. Remote Sens. Environ. 236, 111485 https://doi.org/10.1016/j.rse.2019.111485.

Alerskans, E., Zinck, A.-S.P., Nielsen-Englyst, P., Høyer, J.L., 2022. Exploring machine learning techniques to retrieve sea surface temperatures from passive microwave measurements. Remote Sens. Environ. 281, 113220 https://doi.org/10.1016/j.rse.2022.113220.

AMAP, 2021. Arctic climate change update 2021: Key trends and impacts. In: Summary for Policy-makers. Arctic Monitoring and Assessment Programme (AMAP), Tromsø, Norway.

Andersen, S., Tonboe, R., Kaleschke, L., Heygster, G., Pedersen, L.T., 2007. Intercomparison of passive microwave sea ice concentration retrievals over the high-concentration Arctic Sea ice. J. Geophys. Res. 112, C08004. https://doi.org/10.1029/2006JC003543.

Atkinson, C.P., Rayner, N.A., Kennedy, J.J., Good, S.A., 2014. An integrated database of ocean temperature and salinity observations. J. Geophys. Res. Oceans 119, 7139–7163. https://doi.org/10.1002/2014JC010053.

Banzon, V., Smith, T.M., Steele, M., Huang, B., Zhang, H.-M., 2020. Improved estimation of Proxy Sea surface temperature in the Arctic. J. Atmos. Ocean. Technol. 37, 341–349. https://doi.org/10.1175/JTECH-D-19-0177.1.

Bates, J.J., Diaz, H.F., 1991. Evaluation of multichannel sea surface temperature product quality for climate monitoring: 1982–1988. J. Geophys. Res. 96, 20613. https://doi.org/10.1029/91JC02280.

Bergman, K.H., 1978. Role of observational errors in optimum interpolation analysis. Bull. Am. Meteorol. Soc. 59, 1603–1611. https://doi.org/10.1175/1520-0477-59.12.1603.

Bojinski, S., Verstraete, M., Peterson, T.C., Richter, C., Simmons, A., Zemp, M., 2014. The concept of essential climate variables in support of climate research, applications, and policy. Bull. Am. Meteorol. Soc. 95, 1431–1443. https://doi.org/10.1175/BAMS-D-13-00047.1.

Bretherton, F.P., Davis, R.E., Fandry, C.B., 1976. A technique for objective analysis and design of oceanographic experiments applied to MODE-73. Deep-Sea Res. Oceanogr. Abstr. 23, 559–582. https://doi.org/10.1016/0011-7471(76)90001-2.

Bulgin, C.E., Merchant, C.J., Ferreira, D., 2020. Tendencies, variability and persistence of sea surface temperature anomalies. Sci. Rep. 10, 7986. https://doi.org/10.1038/s41598-020-64785-9.

Carton, J.A., Chepurin, G., Cao, X., Giese, B., 2000. A simple ocean data assimilation analysis of the global upper ocean 1950–95. Part I: method. J. Phys. Oceanogr. 30, 294–309.

Carvalho, K.S., Wang, S., 2020. Sea surface temperature variability in the Arctic Ocean and its marginal seas in a changing climate: patterns and mechanisms. Glob. Planet. Chang. 193, 103265 https://doi.org/10.1016/j.gloplacha.2020.103265.

Castro, S.L., Wick, G.A., Steele, M., 2016. Validation of satellite sea surface temperature analyses in the Beaufort Sea using UpTempO buoys. Remote Sens. Environ. 187, 458–475. https://doi.org/10.1016/j.rse.2016.10.035.

Centurioni, L.R., Turton, J., Lumpkin, R., Braasch, L., Brassington, G., Chao, Y., Charpentier, E., Chen, Z., Corlett, G., Dohan, K., Donlon, C., Gallage, C., Hormann, V., Ignatov, A., Ingleby, B., Jensen, R., Kelly-Gerreyn, B.A., Koszalka, I.M., Lin, X., Lindstrom, E., Maximenko, N., Merchant, C.J., Minnett, P., O'Carroll, A., Paluszkiewicz, T., Poli, P., Poulain, P.-M., Reverdin, G., Sun, X., Swail, V., Thurston, S., Wu, L., Yu, L., Wang, B., Zhang, D., 2019. Global in situ observations of essential climate and ocean variables at the Air-Sea Interface. Front. Mar. Sci. 6, 419. https://doi.org/10.3389/fmars.2019.00419.

Chang, P.S., Jelenak, Z., Alsweiss, S., 2015. Algorithm Theoretical Basis Document: GCOM-W1/AMSR2 Day-1 EDR Version 1.0.

Chelton, D.B., Wentz, F.J., 2005. Global microwave satellite observations of sea surface temperature for numerical weather prediction and climate research. Bull. Am. Meteorol. Soc. 86, 1097–1115. https://doi.org/10.1175/BAMS-86-8-1097.

Chiodi, A.M., Zhang, C., Cokelet, E.D., Yang, Q., Mordy, C.W., Gentemann, C.L., Cross, J. N., Lawrence-Slavas, N., Meinig, C., Steele, M., Harrison, D.E., Stabeno, P.J., Tabisola, H.M., Zhang, D., Burger, E.F., O'Brien, K.M., Wang, M., 2021. Exploring the Pacific Arctic seasonal ice zone with saildrone USVs. Front. Mar. Sci. 8, 640690 https://doi.org/10.3389/fmars.2021.640697.

Cho, K., Sasaki, N., Shimoda, H., Sakata, T., Nishio, F., 1996. Evaluation and improvement of SSM/I sea ice concentration algorithms for the Sea of Okhotsk. J. Remote Sens. Soc. Jpn. 16, 133–144. https://doi.org/10.11440/rssj1981.16.133.

Comiso, J.C., 2003. Warming trends in the Arctic from clear sky satellite observations. J. Clim. https://doi.org/10.1175/1520-0442(2003)016<3498:WTITAF>2.0.CO;2.

Comiso, J.C., Hall, D.K., 2014. Climate trends in the Arctic as observed from space: climate trends in the Arctic as observed from space. WIREs Clim. Change 5, 389–409. https://doi.org/10.1002/wcc.277.

Cowtan, K., Way, R., 2014. Update to "Coverage bias in the HadCRUT4 temperature series and its impact on recent temperature trends". Reconcil. Glob. Temp. Ser. https://doi.org/10.13140/RG.2.1.4334.8564.

Dash, P., Ignatov, A., Martin, M., Donlon, C., Brasnett, B., Reynolds, R.W., Banzon, V., Beggs, H., Cayula, J.-F., Chao, Y., Grumbine, R., Maturi, E., Harris, A., Mittaz, J., Sapper, J., Chin, T.M., Vazquez-Cuervo, J., Armstrong, E.M., Gentemann, C., Cummings, J., Piollé, J.-F., Autret, E., Roberts-Jones, J., Ishizaki, S., Høyer, J.L., Poulter, D., 2012. Group for High Resolution sea Surface Temperature (GHRSST) analysis fields inter-comparisons—Part 2: near real time web-based level 4 SST quality monitor (L4-SQUAM). Deep-Sea Res. II Top. Stud. Oceanogr. 77–80, 31–43. https://doi.org/10.1016/j.dsr2.2012.04.002.

Dee, D.P., Uppala, S.M., Simmons, A.J., Berrisford, P., Poli, P., Kobayashi, S., Andrae, U., Balmaseda, M.A., Balsamo, G., Bauer, P., Bechtold, P., Beljaars, A.C.M., van de Berg, L., Bidlot, J., Bormann, N., Delsol, C., Dragani, R., Fuentes, M., Geer, A.J., Haimberger, L., Healy, S.B., Hersbach, H., Hólm, E.V., Isaksen, L., Kållberg, P., Köhler, M., Matricardi, M., McNally, A.P., Monge-Sanz, B.M., Morcrette, J.-J., Park, B.-K., Peubey, C., de Rosnay, P., Tavolato, C., Thépaut, J.-N., Vitart, F., 2011. The ERA-interim reanalysis: configuration and performance of the data assimilation system. Q. J. R. Meteorol. Soc. 137, 553–597. https://doi.org/10.1002/qj.828.

Dodd, E.M.A., Veal, K.L., Ghent, D.J., Broeke, M.R., Remedios, J.J., 2019. Toward a combined surface temperature data set for the Arctic from the along-track scanning radiometers. J. Geophys. Res. Atmos. 2019JD030262 https://doi.org/10.1029/2019JD030262.

Donlon, C.J., 2020. Copernicus Imaging Microwave Radiometer (CIMR) Mission Requirements Document. Version 4.0.

Donlon, C., Casey, K.S., Gentemann, C., Harris, A., 2010. Successes and challenges for the modern sea surface temperature observing system. In: Proceeding of OceanObs'09: Sustained Ocean Observations and Information for Society.

Donlon, C.J., Martin, M., Stark, J., Roberts-Jones, J., Fiedler, E., Wimmer, W., 2012. The Operational Sea surface temperature and sea ice analysis (OSTIA) system. Remote Sens. Environ. 116, 140–158. https://doi.org/10.1016/j.rse.2010.10.017.

Dybbroe, A., Karlsson, K.-G., Thoss, A., 2005a. NWCSAF AVHRR cloud detection and analysis using dynamic thresholds and radiative transfer modeling. Part I: algorithm description. J. Appl. Meteorol. 44, 39–54. https://doi.org/10.1175/JAM-2188.1.

Dybbroe, A., Karlsson, K.-G., Thoss, A., 2005b. NWCSAF AVHRR cloud detection and analysis using dynamic thresholds and radiative transfer modeling. Part II: tuning and validation. J. Appl. Meteorol. 44, 55–71. https://doi.org/10.1175/JAM-2189.1.

Dybkjær, G., Tonboe, R., Høyer, J.L., 2012. Arctic surface temperatures from metop AVHRR compared to in situ ocean and land data. Ocean Sci. 8, 959–970. https://doi.org/10.5194/os-8-959-2012.

Dybkjær, G., Høyer, J.L., Tonboe, R., Olsen, S.M., 2014. Report on the documentation and description of the new Arctic Ocean dataset combining SST and IST. NACLIM Deliv. D32, 28.

Dybkjær, G., Eastwood, S., Borg, A.L., Høyer, J.L., Tonboe, R., 2018. Algorithm theoretical basis document (ATBD) for the OSI SAF Sea and sea ice surface temperature L2 processing chain. OSI205a and OSI205b.

Dybkjær, G., Eastwood, S., Tonboe, R.T., Nielsen-Englyst, P., Høyer, J.L., Kolbe, W., Jensen, T., Skarpalezos, S., 2022. Arctic and Antarctic Surface Temperatures from AVHRR thermal Infrared satellite sensors 1982-2015; AASTI v2. In prep.

Embury, O., Merchant, C.J., Corlett, G.K., 2012. A reprocessing for climate of sea surface temperature from the along-track scanning radiometers: initial validation, accounting for skin and diurnal variability effects. Remote Sens. Environ. 116, 62–78. https://doi.org/10.1016/j.rse.2011.02.028.

Fiedler, E.K., McLaren, A., Banzon, V., Brasnett, B., Ishizaki, S., Kennedy, J., Rayner, N., Roberts-Jones, J., Corlett, G., Merchant, C.J., Donlon, C., 2019. Intercomparison of long-term sea surface temperature analyses using the GHRSST multi-product ensemble (GMPE) system. Remote Sens. Environ. 222, 18–33. https://doi.org/10.1016/j.rse.2018.12.015.

Folland, C.K., Rayner, N.A., Brown, S.J., Smith, T.M., Shen, S.S.P., Parker, D.E., Macadam, I., Jones, P.D., Jones, R.N., Nicholls, N., Sexton, D.M.H., 2001. Global temperature change and its uncertainties since 1861. Geophys. Res. Lett. 28, 2621–2624. https://doi.org/10.1029/2001GL012877.

Gandin, L.S., 1963. Objective analysis of meteorological field. Gidrometeor. Isdat, Leningrad.

GCOS, 2016. The Global Observing System for Climate: Implementation Needs (No. GCOS-200 (GOOS-214)). World Meteorological Organization (WMO).

Good, S.A., Embury, O., Bulgin, C.E., Mittaz, J., 2019. ESA Sea Surface Temperature Climate Change Initiative (SST_cci): Level 4 Analysis Climate Data Record, Version 2.1. https://doi.org/10.5285/62C0F97B1EAC4E0197A674870AFE1EE6.

Good, S., Fiedler, E., Mao, C., Martin, M.J., Maycock, A., Reid, R., Roberts-Jones, J., Searle, T., Waters, J., While, J., Worsfold, M., 2020. The current configuration of the OSTIA system for operational production of Foundation Sea surface temperature and ice concentration analyses. Remote Sens. 12, 720. https://doi.org/10.3390/rs12040720.

Graversen, R.G., Mauritsen, T., Tjernström, M., Källén, E., Svensson, G., 2008. Vertical structure of recent Arctic warming. Nature 451, 53–56. https://doi.org/10.1038/nature06502.

Hall, D.K., Key, J.R., Case, K.A., Riggs, G.A., Cavalieri, D.J., 2004. Sea ice surface temperature product from MODIS. IEEE Trans. Geosci. Remote Sens. 42, 1076–1087. https://doi.org/10.1109/TGRS.2004.825587.

Hersbach, H., Bell, B., Berrisford, P., Hirahara, S., Horányi, A., Muñoz-Sabater, J., Nicolas, J., Peubey, C., Radu, R., Schepers, D., Simmons, A., Soci, C., Abdalla, S., Abellan, X., Balsamo, G., Bechtold, P., Biavati, G., Bidlot, J., Bonavita, M., Chiara, G., Dahlgren, P., Dee, D., Diamantakis, M., Dragani, R., Flemming, J., Forbes, R., Fuentes, M., Geer, A., Haimberger, L., Healy, S., Hogan, R.J., Hólm, E., Janisková, M., Keeley, S., Laloyaux, P., Lopez, P., Lupu, C., Radnoti, G., Rosnay, P.,

Rozum, I., Vamborg, F., Villaume, S., Thépaut, J., 2020. The ERA5 global reanalysis. Q.J.RMeteorol. Soc. 146, 1999–2049. https://doi.org/10.1002/qj.3803.
Høyer, J.L., Karagali, I., 2016. Sea surface temperature climate data record for the North Sea and Baltic Sea. J. Clim. 29, 2529–2541. https://doi.org/10.1175/JCLI-D-15-0663.1.
Høyer, J.L., She, J., 2007. Optimal interpolation of sea surface temperature for the North Sea and Baltic Sea. J. Mar. Syst. 65, 176–189. https://doi.org/10.1016/j.jmarsys.2005.03.008.
Høyer, J.L., Karagali, I., Dybkjær, G., Tonboe, R., 2012. Multi sensor validation and error characteristics of Arctic satellite sea surface temperature observations. Remote Sens. Environ. 121, 335–346. https://doi.org/10.1016/j.rse.2012.01.013.
Høyer, J.L., Le Borgne, P., Eastwood, S., 2014. A bias correction method for Arctic satellite sea surface temperature observations. Remote Sens. Environ. 146, 201–213. https://doi.org/10.1016/j.rse.2013.04.020.
Hurrell, J.W., Hack, J.J., Shea, D., Caron, J.M., Rosinski, J., 2008. A New Sea surface temperature and sea ice boundary dataset for the community atmosphere model. J. Clim. 21, 5145–5153. https://doi.org/10.1175/2008JCLI2292.1.
Intrieri, J.M., 2002. An annual cycle of Arctic surface cloud forcing at SHEBA. J. Geophys. Res. 107, 8039. https://doi.org/10.1029/2000JC000439.
IPCC, 2019. Special Report on the Ocean and Cryosphere in a Changing Climate..
Jia, C., Minnett, P.J., 2020. High latitude sea surface temperatures derived from MODIS infrared measurements. Remote Sens. Environ. 251, 112094 https://doi.org/10.1016/j.rse.2020.112094.
Kaplan, A., Cane, M.A., Kushnir, Y., Clement, A.C., Blumenthal, M.B., Rajagopalan, B., 1998. Analyses of global sea surface temperature 1856–1991. J. Geophys. Res. 103, 18567–18589. https://doi.org/10.1029/97JC01736.
Kennedy, J.J., 2014. A review of uncertainty in in situ measurements and data sets of sea surface temperature: IN SITU SST UNCERTAINTY. Rev. Geophys. 52, 1–32. https://doi.org/10.1002/2013RG000434.
Kern, S., Lavergne, T., Pedersen, L.T., Tonboe, R.T., Bell, L., Meyer, M., Zeigermann, L., 2022. Satellite passive microwave sea-ice concentration data set intercomparison using landsat data. Cryosphere 16, 349–378. https://doi.org/10.5194/tc-16-349-2022.
Key, J., 1990. Cloud cover analysis with Arctic advanced very high resolution radiometer data: 2. Classification with spectral and textural measures. J. Geophys. Res. 95, 7661. https://doi.org/10.1029/JD095iD06p07661.
Key, J., Maslanik, J.A., Papakyriakou, T., Serreze, M.C., Schweiger, A.J., 1994. On the validation of satellite-Derived Sea ice surface temperature. Arctic 47. https://doi.org/10.14430/arctic1298.
Key, J.R., Collins, J.B., Fowler, C., Stone, R.S., 1997. High-latitude surface temperature estimates from thermal satellite data. Remote Sens. Environ. 61, 302–309. https://doi.org/10.1016/S0034-4257(97)89497-7.
Key, J.R., Mahoney, R., Liu, Y., Romanov, P., Tschudi, M., Appel, I., Maslanik, J., Baldwin, D., Wang, X., Meade, P., 2013. Snow and ice products from suomi NPP VIIRS. J. Geophys. Res. Atmos. 118, 12816–12830. https://doi.org/10.1002/2013JD020459.
Kobayashi, S., Ota, Y., Harada, Y., Ebita, A., Moriya, M., Onoda, H., Onogi, K., Kamahori, H., Kobayashi, C., Endo, H., Miyaoka, K., Takahashi, K., 2015. The JRA-55 reanalysis: general specifications and basic characteristics. J. Meteorol. Soc. Jpn. 93, 5–48. https://doi.org/10.2151/jmsj.2015-001.
Larsen, J., Høyer, J.L., She, J., 2007. Validation of a hybrid optimal interpolation and Kalman filter scheme for sea surface temperature assimilation. J. Mar. Syst. 65, 122–133. https://doi.org/10.1016/j.jmarsys.2005.09.013.
Lavergne, T., Sørensen, A.M., Kern, S., Tonboe, R., Notz, D., Aaboe, S., Bell, L., Dybkjær, G., Eastwood, S., Gabarro, C., Heygster, G., Killie, M.A., Brandt Kreiner, M., Lavelle, J., Saldo, R., Sandven, S., Pedersen, L.T., 2019. Version 2 of the EUMETSAT OSI SAF and ESA CCI Sea-ice concentration climate data records. Cryosphere 13, 49–78. https://doi.org/10.5194/tc-13-49-2019.
Lavergne, T., Kern, S., Aaboe, S., Derby, L., Dybkjær, G., Garric, G., Heil, P., Hendricks, S., Holfort, J., Howell, S., Key, J., Lieser, J., Maksym, T., Maslowski, W., Meier, W.N., Munoz-Sabater, J., Nicolas, J., Özsoy, B., Rabe, B., Rack, W., Raphael, M., de Rosnay, P., Smolyanitsky, V., Tietsche, S., Ukita, J., Vichi, V., Wagner, P., Willmes, S., Zhao, X., 2022. A new structure for the sea ice essential climate variables of the global climate observing system. Under review.
Lenssen, N.J.L., Schmidt, G.A., Hansen, J.E., Menne, M.J., Persin, A., Ruedy, R., Zyss, D., 2019. Improvements in the GISTEMP uncertainty model. J. Geophys. Res. Atmos. 124, 6307–6326. https://doi.org/10.1029/2018JD029522.
Liang, X., Ignatov, A., 2013. AVHRR, MODIS, and VIIRS radiometric stability and consistency in SST bands: AVHRR-MODIS-VIIRS consistency. J. Geophys. Res. Oceans 118, 3161–3171. https://doi.org/10.1002/jgrc.20205.
Liu, Y., Key, J.R., Wang, X., 2008. The influence of changes in cloud cover on recent surface temperature trends in the Arctic. J. Clim. 21, 705–715. https://doi.org/10.1175/2007JCLI1681.1.
Liu, Y., Key, J., Tschudi, M., Dworak, R., Mahoney, R., Baldwin, D., 2015. Validation of the suomi NPP VIIRS ice surface temperature environmental data record. Remote Sens. 7, 17258–17271. https://doi.org/10.3390/rs71215880.
Markus, T., Cavalieri, D.J., 2009. The AMSR-E NT2 Sea Ice Concentration Algorithm : Its Basis and Implementation.
Marquardt Collow, A.B., Cullather, R.I., Bosilovich, M.G., 2020. Recent Arctic Ocean surface air temperatures in atmospheric reanalyses and numerical simulations. J. Clim. 33, 4347–4367. https://doi.org/10.1175/JCLI-D-19-0703.1.
Martin, M., Dash, P., Ignatov, A., Banzon, V., Beggs, H., Brasnett, B., Cayula, J.-F., Cummings, J., Donlon, C., Gentemann, C., Grumbine, R., Ishizaki, S., Maturi, E., Reynolds, R.W., Roberts-Jones, J., 2012. Group for High Resolution sea Surface temperature (GHRSST) analysis fields inter-comparisons. Part 1: a GHRSST multi-product ensemble (GMPE). Deep-Sea Res. II Top. Stud. Oceanogr. 77–80, 21–30. https://doi.org/10.1016/j.dsr2.2012.04.013.
Maslanik, J., Fowler, C., Key, J., Scambos, T., Hutchinson, T., Emery, W., 1997. AVHRR-based polar pathfinder products for modeling applications. Ann. Glaciol. 25, 388–392. https://doi.org/10.3189/S0260305500014336.
Maykut, G.A., 1986. The surface heat and mass balance. In: Untersteiner, N. (Ed.), The Geophysics of Sea Ice. Springer, US, Boston, MA, pp. 395–463. https://doi.org/10.1007/978-1-4899-5352-0_6.
Meier, W.N., 2012. Climate algorithm theoretical basis document (C-ATBD). In: Passive Microwave Sea Ice Concentration. National Oceanic and Atmospheric Administration Climate Data Record Program, Asheville, NC.
Meissner, T., Wentz, F.J., 2012. The emissivity of the ocean surface between 6 and 90 GHz over a large range of wind speeds and earth incidence angles. IEEE Trans. Geosci. Remote Sens. 50, 3004–3026. https://doi.org/10.1109/TGRS.2011.2179662.
Merchant, C.J., Embury, O., Roberts-Jones, J., Fiedler, E., Bulgin, C.E., Corlett, G.K., Good, S., McLaren, A., Rayner, N., Morak-Bozzo, S., Donlon, C., 2014. Sea surface temperature datasets for climate applications from phase 1 of the European Space Agency climate change initiative (SST CCI). Geosci. Data J. 1, 179–191. https://doi.org/10.1002/gdj3.20.
Merchant, C.J., Embury, O., Roberts-Jones, J., Fiedler, E., Bulgin, C.E., Corlett, G.K., Good, S., Rayner, N., Donlon, C., 2016. ESA Sea Surface Temperature Climate Change Initiative (ESA SST CCI): Analysis Long Term Product Version 1.1. https://doi.org/10.5285/2262690A-B588-4704-B459-39E05527B59A.
Merchant, C.J., Paul, F., Popp, T., Ablain, M., Bontemps, S., Defourny, P., Hollmann, R., Lavergne, T., Laeng, A., de Leeuw, G., Mittaz, J., Poulsen, C., Povey, A.C., Reuter, M., Sathyendranath, S., Sandven, S., Sofieva, V.F., Wagner, W., 2017. Uncertainty information in climate data records from earth observation. Earth Syst.Sci. Data 9, 511–527. https://doi.org/10.5194/essd-9-511-2017.
Merchant, C.J., Embury, O., Bulgin, C.E., Block, T., Corlett, G.K., Fiedler, E., Good, S.A., Mittaz, J., Rayner, N.A., Berry, D., Eastwood, S., Taylor, M., Tsushima, Y., Waterfall, A., Wilson, R., Donlon, C., 2019. Satellite-based time-series of sea-surface temperature since 1981 for climate applications. Sci Data 6, 223. https://doi.org/10.1038/s41597-019-0236-x.
Milman, A.S., Wilheit, T.T., 1985. Sea surface temperatures from the scanning multichannel microwave radiometer on Nimbus 7. J. Geophys. Res. 90, 11631. https://doi.org/10.1029/JC090iC06p11631.
Minnett, P.J., Kilpatrick, K.A., Podestá, G.P., Evans, R.H., Szczodrak, M.D., Izaguirre, M.A., Williams, E.J., Walsh, S., Reynolds, R.M., Bailey, S.W., Armstrong, E.M., Vazquez-Cuervo, J., 2020. Skin Sea-surface temperature from VIIRS on suomi-NPP—NASA continuity retrievals. Remote Sens. 12, 3369. https://doi.org/10.3390/rs12203369.
Nielsen-Englyst, P., Høyer, L., Pedersen, J.Toudal, Gentemann, L.L., Alerskans, C., Block, E., Donlon, T., 2018. Optimal estimation of sea surface temperature from AMSR-E. Remote Sens. 10, 229. https://doi.org/10.3390/rs10020229.
Nielsen-Englyst, P., Høyer, J.L., Madsen, K.S., Tonboe, R., Dybkjær, G., Alerskans, E., 2019. In situ observed relationships between snow and ice surface skin temperatures and 2 m air temperatures in the Arctic. Cryosphere 13, 1005–1024. https://doi.org/10.5194/tc-13-1005-2019.
Nielsen-Englyst, P., Høyer, J.L., Madsen, K.S., Tonboe, R.T., Dybkjær, G., Skarpalezos, S., 2021. Deriving Arctic 2 m air temperatures over snow and ice from satellite surface temperature measurements. Cryosphere 15, 3035–3057. https://doi.org/10.5194/tc-15-3035-2021.
O'Carroll, A.G., Armstrong, E.M., Beggs, H.M., Bouali, M., Casey, K.S., Corlett, G.K., Dash, P., Donlon, C.J., Gentemann, C.L., Høyer, J.L., Ignatov, A., Kabobah, K., Kachi, M., Kurihara, Y., Karagali, I., Maturi, E., Merchant, C.J., Marullo, S., Minnett, P.J., Pennybacker, M., Ramakrishnan, B., Ramsankaran, R., Santoleri, R., Sunder, S., Saux Picart, S., Vázquez-Cuervo, J., Wimmer, W., 2019. Observational needs of sea surface temperature. Front. Mar. Sci. 6, 420. https://doi.org/10.3389/fmars.2019.00420.
Ohring, G., Wielicki, B., Spencer, R., Emery, B., Datla, R., 2005. Satellite instrument calibration for measuring global climate change: report of a workshop. Bull. Amer. Meteor. Soc. 86, 1303–1314. https://doi.org/10.1175/BAMS-86-9-1303.
Oke, P.R., Brassington, G.B., Griffin, D.A., Schiller, A., 2008. The Bluelink Ocean data assimilation system (BODAS). Ocean Model. 21, 46–70. https://doi.org/10.1016/j.ocemod.2007.11.002.
Okuro, A., Kubota, M., Tomita, H., Hihara, T., 2014. Inter-comparison of various global sea surface temperature products. Int. J. Remote Sens. 35, 5394–5410. https://doi.org/10.1080/01431161.2014.926415.
Petrenko, B., Ignatov, A., Kihai, Y., Stroup, J., Dash, P., 2014. Evaluation and selection of SST regression algorithms for JPSS VIIRS. J. Geophys. Res. Atmos. 119, 4580–4599. https://doi.org/10.1002/2013JD020637.
Pithan, F., Mauritsen, T., 2014. Arctic amplification dominated by temperature feedbacks in contemporary climate models. Nat. Geosci. 7, 181–184. https://doi.org/10.1038/ngeo2071.
Rantanen, M., Karpechko, A.Yu., Lipponen, A., Nordling, K., Hyvärinen, O., Ruosteenoja, K., Vihma, T., Laaksonen, A., 2022. The Arctic has warmed nearly four times faster than the globe since 1979. Commun. Earth Environ. 3 https://doi.org/10.1038/s43247-022-00498-3.
Rapaić, M., Brown, R., Markovic, M., Chaumont, D., 2015. An evaluation of temperature and precipitation surface-based and reanalysis datasets for the Canadian Arctic, 1950–2010. Atmosphere-Ocean 53, 283–303. https://doi.org/10.1080/07055900.2015.1045825.
Rasmussen, T.A.S., Høyer, J.L., Ghent, D., Bulgin, C.E., Dybkjaer, G., Ribergaard, M.H., Nielsen-Englyst, P., Madsen, K.S., 2018. Impact of assimilation of sea-ice surface

temperatures on a coupled ocean and sea-ice model. J. Geophys. Res. Oceans 123, 2440–2460. https://doi.org/10.1002/2017JC013481.
Rayner, N.A., 2003. Global analyses of sea surface temperature, sea ice, and night marine air temperature since the late nineteenth century. J. Geophys. Res. 108, 4407. https://doi.org/10.1029/2002JD002670.
Rayner, N.A., Auchmann, R., Bessembinder, J., Brönnimann, S., Brugnara, Y., Capponi, F., Carrea, L., Dodd, E.M.A., Ghent, D., Good, E., Høyer, J.L., Kennedy, J.J., Kent, E.C., Killick, R.E., van der Linden, P., Lindgren, F., Madsen, K.S., Merchant, C. J., Mitchelson, J.R., Morice, C.P., Nielsen-Englyst, P., Ortiz, P.F., Remedios, J.J., van der Schrier, G., Squintu, A.A., Stephens, A., Thorne, P.W., Tonboe, R.T., Trent, T., Veal, K.L., Waterfall, A.M., Winfield, K., Winn, J., Woolway, R.I., 2020. The EUSTACE project: delivering global, daily information on surface air temperature. Bull. Am. Meteorol. Soc. 101, E1924–E1947. https://doi.org/10.1175/BAMS-D-19-0095.1.
Reynolds, R.W., Smith, T.M., 1994. Improved Global Sea surface temperature analyses using optimum interpolation. J. Clim. 7, 929–948. https://doi.org/10.1175/1520-0442(1994)007<0929:IGSSTA>2.0.CO;2.
Reynolds, R.W., Rayner, N.A., Smith, T.M., Stokes, D.C., Wang, W., 2002. An improved in situ and satellite SST analysis for climate. J. Clim. 15, 1609–1625. https://doi.org/10.1175/1520-0442(2002)015<1609:AIISAS>2.0.CO;2.
Reynolds, R.W., Smith, T.M., Liu, C., Chelton, D.B., Casey, K.S., Schlax, M.G., 2007. Daily high-resolution-blended analyses for sea surface temperature. J. Clim. 20, 5473–5496. https://doi.org/10.1175/2007JCLI1824.1.
Richter-Menge, J.A., Overland, J., Mathis, J.T., Osborne, E., 2017. Arctic Report Card 2017.
Roberts-Jones, J., Fiedler, E.K., Martin, M.J., 2012. Daily, global, high-resolution SST and sea ice reanalysis for 1985–2007 using the OSTIA system. J. Clim. 25, 6215–6232. https://doi.org/10.1175/JCLI-D-11-00648.1.
RU/FSR/HME/AARI, NSIDC, 1993. AARI Russian North Polar Drifting Station Data, from NSIDC. https://doi.org/10.5065/V47S-KW40.
Serreze, M.C., Box, J.E., Barry, R.G., Walsh, J.E., 1993. Characteristics of Arctic synoptic activity, 1952–1989. Meteorl. Atmos. Phys. 51, 147–164. https://doi.org/10.1007/BF01030491.
Shibata, A., 2006. Features of ocean microwave emission changed by wind at 6 GHz. J. Oceanogr. 62, 321–330. https://doi.org/10.1007/s10872-006-0057-3.
Simmons, A.J., 2004. Comparison of trends and low-frequency variability in CRU, ERA-40, and NCEP/NCAR analyses of surface air temperature. J. Geophys. Res. 109, D24115. https://doi.org/10.1029/2004JD005306.
SMHI, 2014. Algorithm Theoretical Basis Document for the Cloud Mask of the NWC/PPS. NWC/CDOP2/PPS/SMHI/SCI/ATBD/1, Issue 1, Rev. 0.
Song, X., Yu, L., 2012. High-latitude contribution to global variability of Air-Sea sensible heat flux. J. Clim. 25, 3515–3531. https://doi.org/10.1175/JCLI-D-11-00028.1.
Studinger, M., 2020. IceBridge KT19 IR Surface Temperature, Version 2. https://doi.org/10.5067/UHE07J35I3NB.
Timmermans, M.-L., Labe, Z., 2020. Arctic Report Card 2020: Sea Surface Temperature. https://doi.org/10.25923/V0FS-M920.
Tonboe, R.T., Dybkjær, G., Høyer, J.L., 2011. Simulations of the snow covered sea ice surface temperature and microwave effective temperature. Tellus A 63, 1028–1037. https://doi.org/10.1111/j.1600-0870.2011.00530.x.
Tonboe, R.T., Eastwood, S., Lavergne, T., Sørensen, A.M., Rathmann, N., Dybkjær, G., Pedersen, L.T., Høyer, J.L., Kern, S., 2016. The EUMETSAT Sea ice concentration climate data record. Cryosphere 10, 2275–2290. https://doi.org/10.5194/tc-10-2275-2016.
Vazquez-Cuervo, J., Castro, S.L., Steele, M., Gentemann, C., Gomez-Valdes, J., Tang, W., 2022. Comparison of GHRSST SST analysis in the Arctic Ocean and alaskan coastal waters using saildrones. Remote Sens. 14, 692. https://doi.org/10.3390/rs14030692.
Vincent, R.F., Marsden, R.F., Minnett, P.J., Buckley, J.R., 2008a. Arctic waters and marginal ice zones: 2. An investigation of arctic atmospheric infrared absorption for advanced very high resolution radiometer sea surface temperature estimates. J. Geophys. Res. 113, C08044. https://doi.org/10.1029/2007JC004354.
Vincent, R.F., Marsden, R.F., Minnett, P.J., Creber, K.A.M., Buckley, J.R., 2008b. Arctic waters and marginal ice zones: a composite Arctic Sea surface temperature algorithm using satellite thermal data. J. Geophys. Res. 113, C04021. https://doi.org/10.1029/2007JC004353.
Walsh, J.E., Chapman, W.L., 1998. Arctic Cloud–Radiation–Temperature associations in observational data and atmospheric reanalyses. J. Clim. 11, 3030–3045. https://doi.org/10.1175/1520-0442(1998)011<3030:ACRTAI>2.0.CO;2.
Wang, X., Key, J.R., 2005. Arctic surface, cloud, and radiation properties based on the AVHRR polar pathfinder dataset. Part II: recent trends. J. Clim. 18, 2575–2593. https://doi.org/10.1175/JCLI3439.1.
Wang, H., Guan, L., Chen, G., 2016. Evaluation of sea surface temperature from FY-3C VIRR data in the Arctic. IEEE Geosci. Remote Sens. Lett. 13, 292–296. https://doi.org/10.1109/LGRS.2015.2511184.
Wentz, F.J., Meissner, T., 2000. AMSR Ocean Algorithm. Algorithm Theoretical Basis Document (No. Version 2). Remote Sensing Systems, Santa Rosa, CA.
Wentz, F.J., Gentemann, C., Smith, D., Chelton, D.B., 2000. Satellite measurements of sea surface temperature through clouds. Science 288, 847–850. https://doi.org/10.1126/science.288.5467.847.
White, W.B., 1995. Design of a global observing system for gyre-scale upper ocean temperature variability. Prog. Oceanogr. 36, 169–217. https://doi.org/10.1016/0079-6611(95)00017-8.